

Observing the Time Evolution of the Multi-Component Nucleus of 3C 84

BRIAN PUNSLEY,^{1,2,3} HIROSHI NAGAI,^{4,5} TUOMAS SAVOLAINEN,^{6,7,8} AND MONICA ORIENTI⁹

¹*1415 Granvia Altamira, Palos Verdes Estates CA, USA 90274*

²*ICRANet, Piazza della Repubblica 10 Pescara 65100, Italy*

³*ICRA, Physics Department, University La Sapienza, Roma, Italy*

⁴*National Astronomical Observatory of Japan, Osawa 2-21-1, Mitaka, Tokyo 181-8588, Japan*

⁵*The Graduate University for Advanced Studies, SOKENDAI, Osawa 2-21-1, Mitaka, Tokyo 181-8588, Japan*

⁶*Aalto University Metsähovi Radio Observatory, Metsähovintie 114, 02540 Kylmälä, Finland*

⁷*Aalto University Department of Electronics and Nanoengineering, PL 15500, 00076 Aalto, Finland*

⁸*Max-Planck-Institut für Radioastronomie, Auf dem Hügel 69, 53121 Bonn, Germany*

⁹*INAF - Istituto di Radioastronomia, Via Gobetti 101, 40129 Bologna, Italy*

(Received ...; Revised ...; Accepted ...)

Submitted to ApJ

ABSTRACT

The advent of global mm-band Very Long Baseline Interferometry (VLBI) in recent years has finally revealed the morphology of the base of the two most prominent nearby, bright, extragalactic radio jets in M87 and 3C 84. The images are quite surprising considering the predictions of jet theory and current numerical modeling. The jet bases are extremely wide compared to expectations and the nucleus of 3C 84 is very complicated. It appears as a double in 86 GHz observations with $50 \mu\text{as}$ resolution and a triple nucleus with $30 \mu\text{as}$ resolution with space-based VLBI by RadioAstron at 22 GHz. What is even odder is that the double and triple are arranged along an east-west line that is approximately orthogonal to the north-south large scale jet on $150 \mu\text{as} - 4 \text{mas}$ scales. We explore the emergence of an (east-west) double nucleus in the lower resolution 43 GHz Very Long Baseline Array (VLBA) imaging from August 2018 to April 2020. The double is marginally resolved. We exploit the east-west resolution associated with the longest baselines, $\sim 0.08 \text{mas}$, to track a predominantly east-west separation speed of $\approx 0.086 \pm 0.008 c$. We estimate that the observed mildly relativistic speed persists over a de-projected distance of $\sim 1900 - 9800$ times the central, supermassive black hole, gravitational radius ($\sim 0.3 - 1.5 \text{lt-yr}$) from the point of origin.

Keywords: black hole physics — galaxies: jets—galaxies: active — accretion, accretion disks

1. INTRODUCTION

The galaxy, NGC 1275, harbors the radio source 3C 84 with both a parsec scale jet and a kpc scale jet as well as a large low frequency radio halo (Pedlar et al. 1990; Walker et al. 2000). It has been the brightest extragalactic radio source at high frequency with flux densities of 45 Jy – 65 Jy in 1980 at 270 GHz and $\sim 40 - 50$ Jy at 90 GHz from 1965–1985 (Nesterov et al. 1995). The flare subsided in the 1990s, but a new strong flare began in 2005 (Nagai et al. 2010; Trippe et al. 2011). Due to its proximity ($z = 0.0176$), and its brightness, 3C 84 along with M 87 are the best candidates for resolving the jet near the launching region with high frequency Very Long Baseline Interferometry (VLBI). High resolution observations of M 87 and 3C 84 have displayed extremely wide jet opening angles within 0.1 mas of the core, $\sim 127^\circ$ and 138° , respectively and both jets are extremely edge brightened near the base (Kim et al. 2018; Giovannini et al. 2018; Punsly 2019). The large degree of edge brightening and the enormous (the maximum possible geometrically is 180°) opening angles were not anticipated in seminal works on simple jet theory (Blandford and Königl 1979). Numerical models of jet formation have been designed to explain these extreme properties in M 87. It was hoped that choosing lines of sight (LOS) that are nearly aligned with the jet axis and plasma emissivity/plasma enthalpy profiles (injected by numerical researchers) that were specifically designed to produce the high resolution radio images would resolve the conflict (Mościbrodzka et al. 2016; Chael et al. 2019). However, current numerical simulations still produce synthetic jet images that are far too narrow and not nearly edge brightened enough near their bases when compared directly to the highest resolution interferometric images of the jet base (Punsly 2019). This wide base seems to abruptly transition to a highly collimated inner jet. The powerlaw fit to the jet width, $W(z)$, as a function of axial displacement along the jet, z , is $W(z) \propto z^k$, $k = 0.230 \pm 0.049$ for $0.06\text{mas} < z < 0.3\text{mas}$ in M 87, even though the jet might be parabolic ($k=0.5$) at larger z (Punsly 2019). A similar abrupt transition also seems to occur in the jet of 3C 84 juxtaposed to its wide base, see Giovannini et al. (2018) or Figures 9 and 10 of this paper. Furthermore, 3C 84 was shown to have a triple nucleus in the highest resolution radio observation, $30 \mu\text{as}$, performed with RadioAstron at 22GHz^1 (Giovannini et al. 2018). The triple is distributed primarily along the east-west direction roughly orthogonal to the jet that is directed towards the south and is defined by two bright ridges, beginning $150 \mu\text{as}$ to the south (see the schematic diagram in Figure 1). These circumstances suggest that there is jet launching physics to be discovered with high resolution of VLBI, and not just the verification of existing theory.

Thus motivated, this study explores the nature of the multi-component nucleus that has been seen with the highest resolution VLBI, $\sim 30 \mu\text{as}$ in the east-west direction with RadioAstron on September 21-22, 2013 (Giovannini et al. 2018). Our method is to use the lower resolution 7 mm Very Long Baseline Array (VLBA) data that is created for the purpose of approximately monthly monitoring by a Boston University based research effort, the VLBA-BU Blazar Monitoring Program² (Jorstad et al. 2017). Thus, we can, in principle, detect time evolution of the nuclear region. A partially resolved double nucleus has appeared in the CLEAN images from August 26, 2018 to April 7, 2020. We rely on the publicly available files from the BU website to extract the highest resolution data, corresponding to the longest baselines associated with the 43 GHz VLBA.

¹ We define the multiplicity of the nucleus, i.e. double or triple, as the apparent number of components that can be discerned from visual inspection of the image. This designation is a function of the resolution of the telescope. If the resolution were much higher then there could be many small components that could not be seen at lower resolution.

² <http://www.bu.edu/blazars/VLBAproject.html>

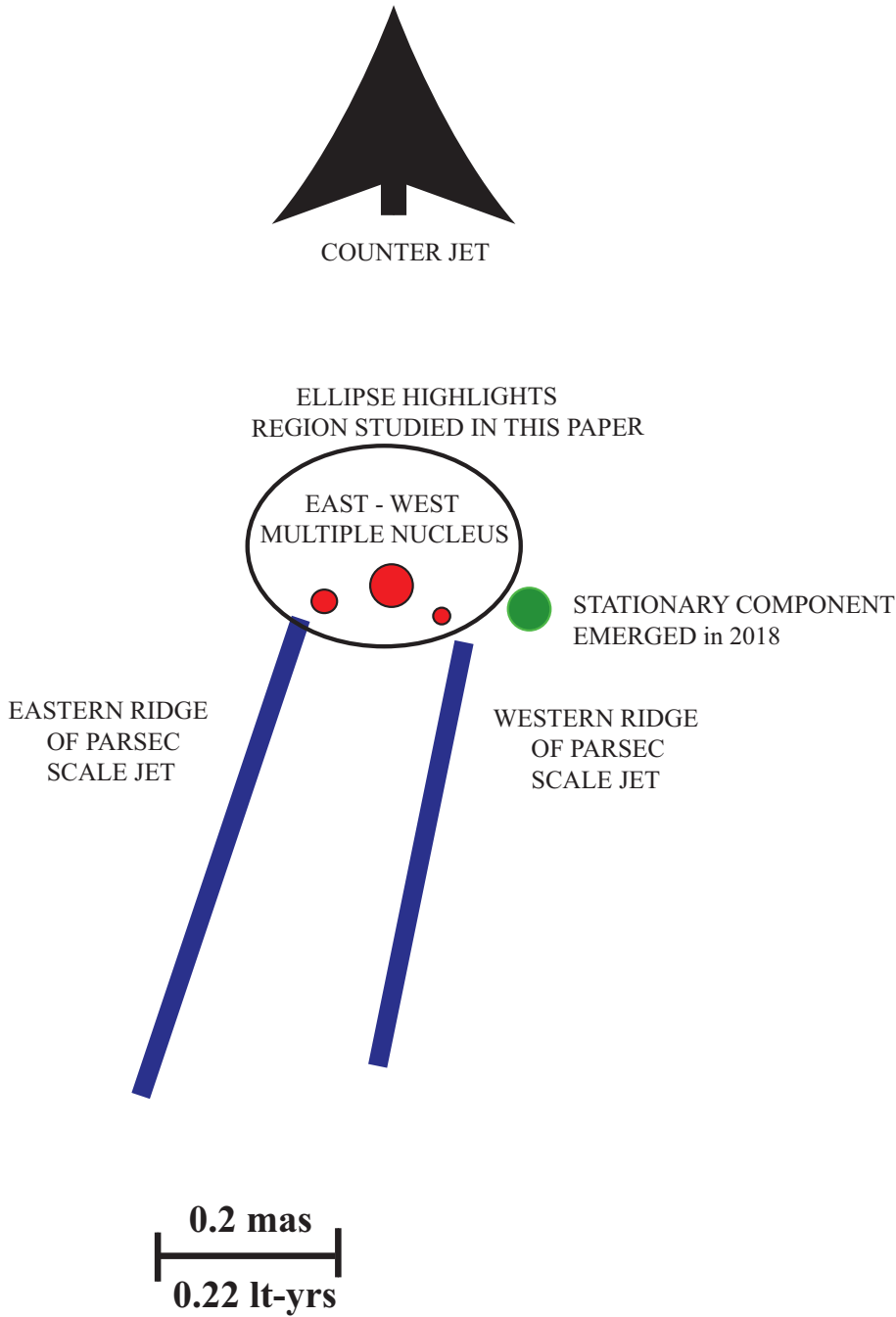


Figure 1. The taxonomy of prominent features in the nuclear region of 3C 84. The position angle of the southerly directed jet swings back and forth from east to west by $\sim 35^\circ$ over periods of about 5-10 years.

We begin with a description of the very complex nuclear inner light year of the jet that has been revealed in recent high resolution VLBI campaigns. Figure 1 is a schematic diagram of the numerous nuclear features that have been detected in this nearby very bright radio source. A schematic is much clearer than overlaying numerous images made at various frequencies. An approximate scale is indicated at the bottom, both in angular size and physical dimension (projected on the sky plane). The primary feature is the triple nucleus (enclosed by the ellipse) from the 22 GHz RadioAstron

observations (Giovannini et al. 2018). This region is the focus of this study. This nuclear feature is apparently not time stationary. A more recent 86 GHz global VLBI observation on May 16, 2015 revealed this region to be a double nucleus along the east-west direction (Kim et al. 2019). With 43 GHz VLBA, a double nucleus has never been identified previously. Based on the aforementioned higher resolution VLBI, the east-west separation is $\sim 0.1 - 0.15$ mas, similar to the nominal east-west restoring beam of the uniformly weighted 10 station VLBA of 0.15 mas. Thus, we expect to see partially resolved structure in epochs of wide separation.

Figure 1 shows other complicating features as well and helps to illustrate the ultimate goal of finding a unifying picture that incorporates all of these important elements. First, there is the faint counter-jet that has been seen at numerous frequencies (Walker et al. 2000; Lister 2001; Fujita and Nagai 2017). Then there are the very prominent east and west ridges that frame the jet headed to the south. They are of varied prominence from epoch to epoch and observation to observation. In the high resolution 22 GHz RadioAstron observation they are significantly brighter than the almost hollow interior of the jet. This “double rail” configuration has also been seen with 43 GHz VLBA (Nagai et al. 2014). A similar double rail configuration has been detected in high resolution VLBI images of M 87 adjacent to the nucleus as well (Hada et al. 2014; Kim et al. 2018). The most curious aspect of these ridges in the 43 GHz BU VLBA monitoring data is that most of the time one ridge is much brighter than the other for periods of time that last years. The fundamental question that we wish to gain some insight into is: what is the relationship between the multiple east-west nucleus and these vacillating bright ridges of emission that emerge almost orthogonal to the axis of nuclear emission, in the southern direction?

Some of these features are evident in the magnified views of the nuclear region from the total intensity images taken from the BU website in Figure 2. We note one other aspect of the nuclear region. A modest feature has emerged to the west of the nucleus in 2018, about 0.25 mas away. It appears to be real because it is persistent and is seen a few contours above the noise level. It also seems to be stationary. With all the components emerging in almost every direction, the situation is not well explained by a simple pencil-beam jet. We are actually getting close to the jet launching region, so we are starting to uncover some of the messy details of the physical mechanism. We do not attempt to resolve these complexities in the present paper. We take a more modest approach and merely try to establish and quantify the rate of nuclear expansion within the central ellipse of Figure 1.

Section 2 describes our methods of extracting the nuclear separation from the data. In Section 3, we describe how we use the CLEAN component (CC) models from the BU program to extract the east-west resolution associated with the longest baselines. Section 4 presents our estimate of the apparent speed of separation of the double nucleus. In Section 5, we explore the non-trivial methods of fitting the nuclear components in the (u, v) plane using Gaussian models. In Section 6, we compare the nuclear configuration observed by the 43 GHz VLBA in 2018-2020 with the nuclear triple observed by RadioAstron in 2013. Throughout this paper, we adopt the following cosmological parameters: $H_0=69.6$ km s $^{-1}$ Mpc $^{-1}$, $\Omega_\Lambda = 0.714$ and $\Omega_m = 0.286$ and use Ned Wright’s Javascript Cosmology Calculator website (Wright 2006). In our adopted cosmology we use a conversion of 0.360 pc to 1 mas.

2. METHOD OF ESTIMATING NUCLEAR EXPANSION

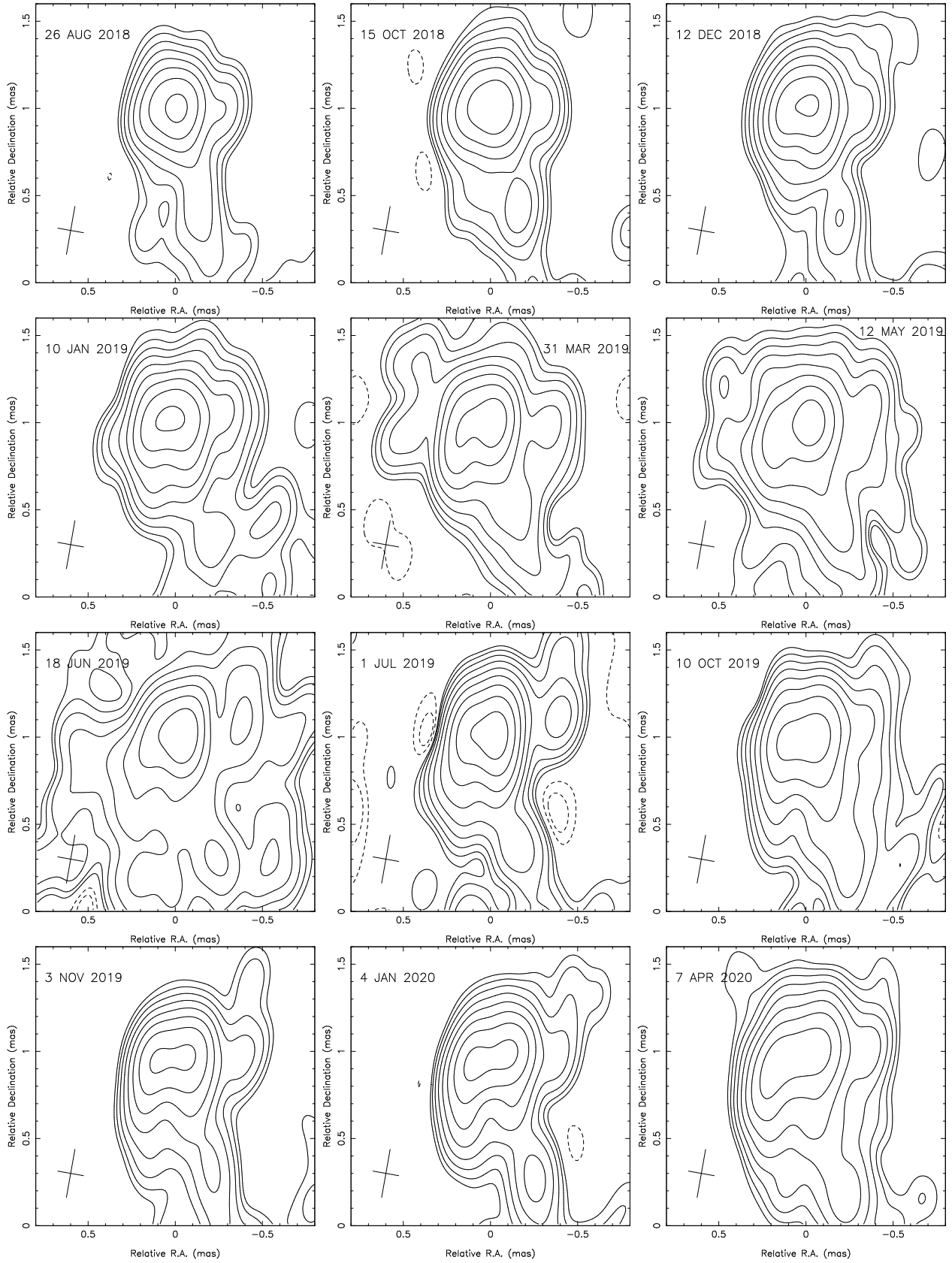


Figure 2. The nucleus in the 43 GHz image starts elongating in the east-west direction in August 2018. The nucleus appears almost fully resolved by November 2019. The eastern component seems to veer towards the large scale southerly directed jet in the 2020 images. The details of the degree of degradation of many compromised observations in 2019 can be found in Table 1. The June and July 2019 images reflect the significant degradation indicated in Table 1. The contours start from 10 mJy/beam and increase in steps of 2x in all the plots. The restoring beam is indicated by the cross in the lower left.

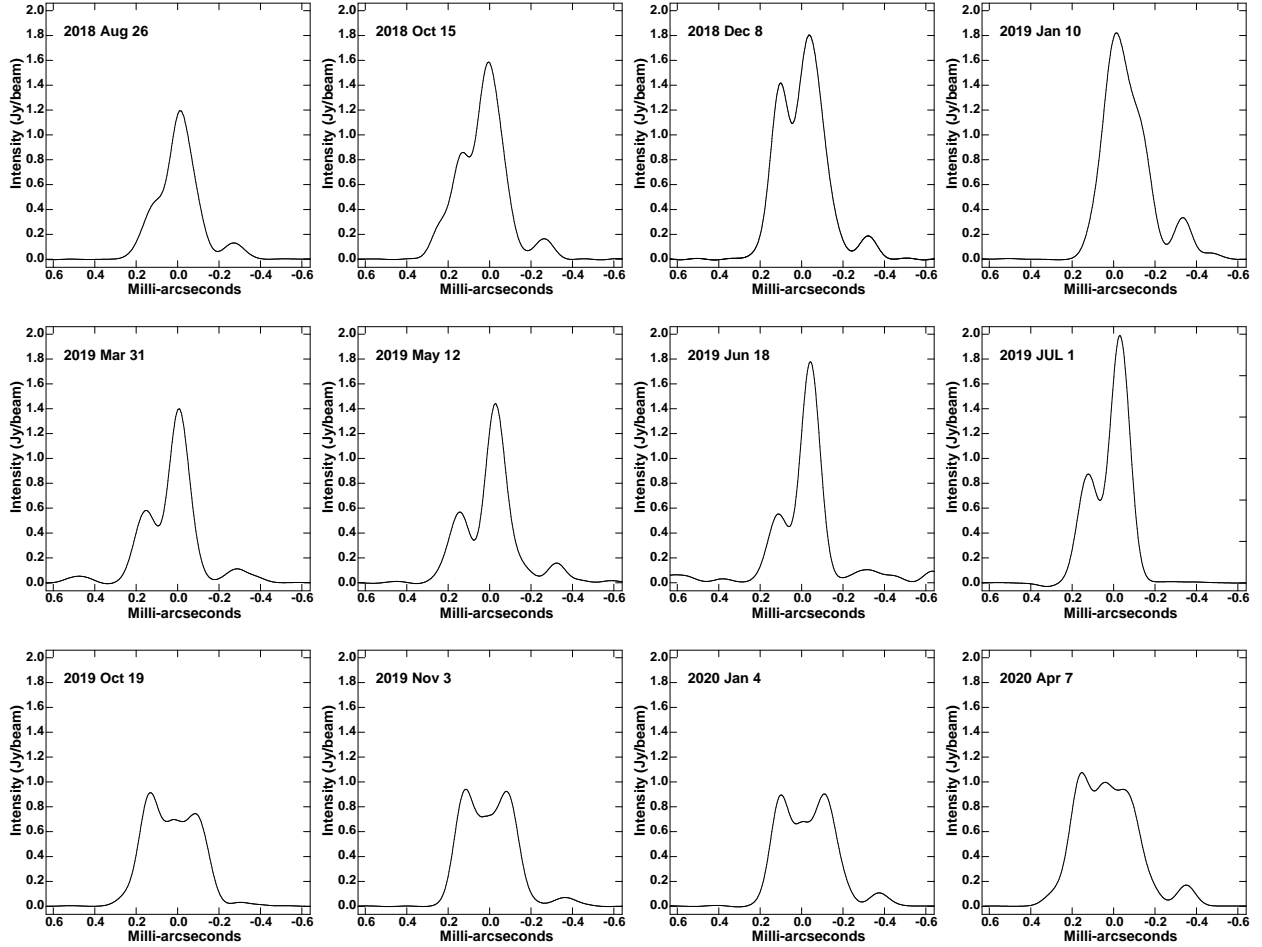


Figure 3. East-west intensity cross sections created from the CLEAN images. They are fixed in the north-south direction by locating them to pass through the peak intensity. Notice the emergence of a local maximum to the east of the peak on August 26, 2018. A double peak is clearly seen on October 15, 2018. A third local maximum emerges in October 2019. Notice that January 10, 2019 has a different cross-section with just a single peak. This epoch requires special attention (see Appendix B).

It is fortuitous that the nucleus expands primarily in the east-west direction, this is also the direction of maximum resolution of the VLBA at 43 GHz (the major axis of the restoring beam has a position angle of -10°). The full width at half maximum (FWHM) of the beam is approximately $0.28 \text{ mas} \times 0.15 \text{ mas}$ for uniformly weighted (u, v) data. However, when the data have sufficiently high signal-to-noise ratio, the interferometer can resolve structures significantly smaller than the nominal beam size. In our case the longest baselines provide a typical resolution of approximately 0.08 mas in the east-west direction. The resolution of the interferometer is defined here as the FWHM of a circular Gaussian brightness distribution that gives a visibility amplitude of 50% times the zero-baseline value. Mathematically, this is expressed as $\text{resolution} = (91M\lambda/\text{baseline-length}) \text{ mas}$ (Marscher 1985). It is known that higher resolution can be achieved by analyzing the visibility domain and these resolution limits depend on the noise in the (u, v) plane (Marti-Vidal et al. 2012). However, working in the image plane has the advantage of less ambiguity as to whether the model chosen for the source is appropriate (Fomalont 1999). Since we are measuring small changes to a small separation on a

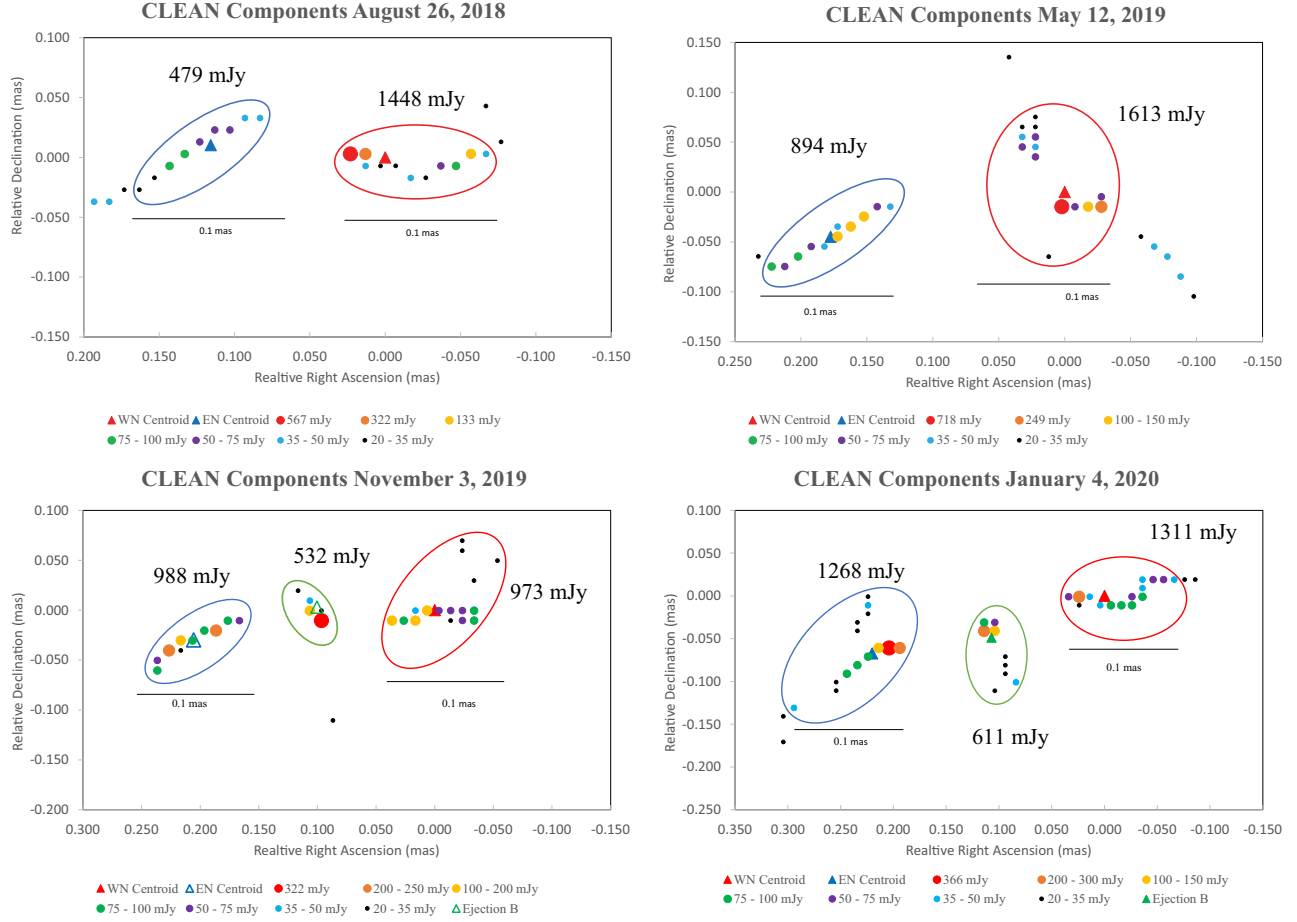


Figure 4. The location of the nuclear CCs in four epochs. The two examples in the top row are used to illustrate our methods of defining which CCs determine the WN and EN. The WN and EN are defined by the CCs enclosed within red and blue ellipses, respectively. The red and blue triangles are the corresponding centroids of the flux density for each physical component. The details of these constructions are provided in the text. Note that the CCs outside the solid ellipses are weak (20–35 mJy) and do not affect the centroid estimates, but we cut the CC distribution off once it approaches 0.1 mas in east-west width as motivated in the text. The two examples in the bottom row show the emergence of a weaker (green) component in the fall of 2019. We consider EN as the first ejection, ejection A, and the green cluster of CCs as a second ejection, ejection B.

complex background, the ambiguities in the models can cause a significant degradation of accuracy. In Appendix A, we provide simulations in the visibility domain to motivate the Marscher (1985) resolution limit as appropriate to this study. These simulations incorporate all the details of the observations that degrade the very high resolution limits achievable with model-fitting the visibility data with near perfect circumstances. We incorporate the (u, v) coverage, SNR, and the complexity of the source structure. Even though this analysis is in the (u, v) plane, “analysis of a properly made CLEAN image via good analysis techniques should produce values and errors which are equal to those of model fitting visibility data” (Fomalont 1999). The CLEAN component based method utilized in this paper will be shown to be an example of a “good analysis technique” in the image plane. We are able to find Gaussian fitting methods in Section 5 that yield similar resolution limits to our CLEAN

Table 1. Compromised Observations in 2019

Date	Missing Stations	Severely Compromised Stations	Comments	Quality
02/03/2019	MK and BR	...	east-west resolution severely degraded	un-useable
02/08/2019	NL	BR and HN much data deleted due to bad weather	only ~ 7 stations disperses the distribution of CCs in image plane	un-useable
03/31/2019	HN	LA missing half of the data	good east-west resolution from SC and MK, low SNR	useable
05/12/2019	SC	...	MK and HN still provided good east-west resolution	useable
06/18/2019	SC	...	inaccurate pointing of the antennae, low SNR	useable
07/01/2019	SC	...	inaccurate pointing of the antennae, low SNR	useable
10/19/2019	BR	...	low SNR	useable

NOTE—Details of the observations generously provide by A. Marscher, 2019. Station acronyms: MK (Mauna Kea), BR (Brewster, Washington), NL (North Liberty, Iowa), HN (Hancock, New Hampshire), LA (Los Alamos, New Mexico), SC (St. Croix)

component based methods. This forms a bridge between the simulations in Appendix A and the CLEAN component based method presented here.

So, in theory, there is information within the observations that can resolve east-west features larger than 0.1 mas , provided their signal-to-noise ratio (SNR) is high. The $0.28 \text{ mas} \times 0.15 \text{ mas}$ uniformly weighted restoring beam is too large to do this cleanly, the resultant blurring prevents a clear east-west determination. The images in Figure 2 show this to be the case as there appears to be two heavily blurred components that are separating over time. We need to extract these partially resolved structures from the observations in order to quantify the east-west separation over time. There are three possible methods, super-resolved images based on a restoring beam smaller than the central peak of the conventional interferometer beam, direct analysis of the clean component (CC) model, and fitting the visibilities with simple models of the core structure. The super-resolved images highlight the multiple nucleus, but create large artifacts at angles more than 45° from the east-west direction. The net result is a suggestive image, but Gaussian fits to the multiple components fail to converge to a unique decomposition. The same circumstance exists with efforts to fit the visibilities with simple Gaussian models (see Section 5). The other alternative is to use the CC models. Even though the models cannot be considered robust in a single epoch, they should be suitable for identifying a trend that persists over time, especially with regards to very bright features as is the case here. This is the primary guiding principle of the following analysis.

Before describing our models we first note that most observations in 2019 are degraded to varying degrees by bad weather, down observing stations and inaccurate antennae pointing. The issues are summarized in Table 1. Modest degradation of observations in 2019 adversely affect the CC models

and one of the main tasks of this analysis is to quantify this degradation in terms of an uncertainty in our results.

In order to transition from the images in Figure 2 to the CC models, we investigate intensity profiles of the CLEAN image along a particular direction (east-west). We define a pixel size as $0.005 \text{ mas} \times 0.005 \text{ mas}$. We center an array of pixels on the peak of the intensity. We place a circular Gaussian beam with a 0.1 mas FWHM at the location of peak intensity and measure the intensity. This is about 25% larger angular resolution than the angular resolution of the longest baselines of the array. We then slide the circular Gaussian beam to the east and the west in discrete 0.005 mas increments in order to generate the intensity cross-sections in Figure 3. The intensity profiles were generously provided by Alan Marscher. There is a clear local maximum to the east of the peak on August 26, 2018. This corresponds to the slight elongation towards the east in the first panel of Figure 2. A double peak is clearly seen on October 15, 2018 and December 9, 2018 which appears as increasing elongation of the nucleus towards the east in Figure 2. The spacing between the peaks keeps increasing and on March 31, 2019 and May 12, 2019 there is clearly two distinct components in the image plane. Notice that January 10, 2019 has a different cross-section with just a single peak. This is out of family with the other epochs, including the epoch just before and the epoch just after in December and in March, respectively. Consequently, we analyze this observation separately in Appendix B in order to assess the reason that the uniform cross-sectional procedure failed to pick up the second peak and nature of the root cause.

3. THE CLEAN COMPONENT MODELS

CC models are provided for each observation epoch on the BU website. During the first year of monitoring in Figure 2, the western component of the double nucleus (WN, hereafter) is brighter and fortunately is predominantly a tight east-west distribution of the bright CCs that always includes the brightest CC. We face two primary technical issues that we illustrate in Figure 4 with four examples. The issues are:

1. How should the cluster of components be defined for both the eastern component of the nucleus (EN, hereafter) and the WN?
2. How do we define the coordinates of the cluster of components and the uncertainty in this location?

We explore these issue below.

3.1. *Defining the Clustering of the CLEAN Components*

This is a slightly subjective exercise at times in which we use the visual evidence from Figures 2 and 3 and the structure of the components in the previous epoch and the subsequent epoch. The peak surface brightness is about $1.5 - 3.0 \text{ Jy/beam}$ in each image. We consider any CC with a flux density larger than $\sim 20 - 35 \text{ mJy}$ as significant. This varies depending on the quality of the observation. This choice typically scales with the magnitude of the strongest negative contour in the FITS image file (see Table 2). In practice, components less than 40 mJy never contribute significantly to our flux density related results (component centroids and uncertainties). Figure 4 plots all the components larger than 20 mJy in the vicinity of the nucleus in four epochs. The red ellipse defines all the components that we associate with the WN and the blue ellipse encapsulates all

Table 2. Details of the CLEAN Component Models of the Double Nucleus

(1)	(2)	(3)	(4)	(5)	(6)	(7)	(8)	(9)	(10)	(11)
Date	Day	$F_{\nu, \text{WN}}$	$F_{\nu, \text{EN}}$	Uniformly Weighted Beam (Naturally Weighted Beam)	I_{peak}	Min. Neg.	Smallest	ΔRA	Δdec	Separation
		(Jy)	(Jy)	Size/PA (mas/degrees)	(Jy/beam)	Cont. (mJy/beam)	CC (mJy)	(mas)	(mas)	(mas)
08/26/2018	0	1.448	0.479	$0.303 \times 0.179/+11.0$ ($0.370 \times 0.231/+13.3$)	1.572	-15	20	0.116 ± 0.013	0.010 ± 0.021	0.116 ± 0.013
10/15/2018	50	1.856	0.838	$0.314 \times 0.154/+3.6$ ($0.352 \times 0.175/+1.1$)	2.462	-14	25	0.133 ± 0.011	0.001 ± 0.022	0.133 ± 0.011
12/09/2018	105	2.707	1.441	$0.345 \times 0.166/+14.9$ ($0.381 \times 0.190/+10.3$)	2.875	-10	20	0.144 ± 0.013	-0.030 ± 0.024	0.147 ± 0.014
01/10/2019	137	3.349	1.079	$0.361 \times 0.160/+21.4$ ($0.405 \times 0.187/+21.0$)	2.974	-15	20	0.147 ± 0.014	-0.075 ± 0.024	0.165 ± 0.017
03/31/2019	217	1.325	0.901	$0.306 \times 0.153/+8.9$ ($0.344 \times 0.185/+7.4$)	2.204	-24	25	0.175 ± 0.011	-0.031 ± 0.021	0.178 ± 0.012
05/12/2019	259	1.356	0.894	$0.407 \times 0.176/-13.2$ ($0.435 \times 0.197/-10.8$)	2.064	-17	20	0.178 ± 0.014	-0.045 ± 0.028	0.183 ± 0.015
06/18/2019	296	2.337	0.799	$0.397 \times 0.183/-16.4$ ($0.432 \times 0.211/-14.5$)	2.462	-29	35	0.173 ± 0.015	0.003 ± 0.027	0.173 ± 0.015
07/01/2019	309	3.448	2.116	$0.425 \times 0.173/-14.3$ ($0.434 \times 0.210/-12.9$)	4.030	-36	35	0.149 ± 0.014	0.019 ± 0.029	0.150 ± 0.014
10/19/2019	419	0.793	0.823	$0.329 \times 0.142/-5.2$ ($0.386 \times 0.159/-8.3$)	1.840	-29	35	0.193 ± 0.010	-0.043 ± 0.023	0.198 ± 0.011
11/03/2019	434	0.973	0.988	$0.318 \times 0.153/+3.6$ ($0.387 \times 0.183/+0.6$)	1.490	-13	20	0.206 ± 0.011	-0.030 ± 0.022	0.208 ± 0.011
01/04/2020	496	1.311	1.268	$0.330 \times 0.165/+2.1$ ($0.399 \times 0.205/+0.1$)	1.633	-13	20	0.220 ± 0.012	-0.067 ± 0.023	0.230 ± 0.013
04/07/2020	590	1.634	1.613	$0.316 \times 0.144/+4.5$ ($0.342 \times 0.160/+6.4$)	2.127	-10	20	0.238 ± 0.010	-0.068 ± 0.022	0.248 ± 0.012

the components associated with the EN. We crudely estimate that the east-west spread of the CCs in the WN and EN will be distributed within a length < 0.1 mas. This follows from de-convolving the 0.1 mas FWHM restoring beam from the FWHM of the intensity cross-sections peaks in Figure 3. We get 20 estimates of the FWHM of peaks that range from 0.023 mas to 0.112 mas with a mean of 0.076 mas. Truncating the east-west width of the CC distribution < 0.1 mas is the fundamental constraint for estimating which components should be included in the WN and EN. This approximate limit guarantees that the size of the distributions of CCs in the EN and WN are small enough that the nuclear components can be clearly differentiated in our efforts to estimate separations as small as 0.1 mas. If this condition is not obeyed by the data then the CC clustering method cannot be used to measure the smallest separations, ~ 0.1 mas. A priori we do not know if this assumption is consistent with the data. Ultimately, this assumption is verified empirically. For example, we present 7 CC scatter plots of the nuclear region in Figures 4, 7, 8 and 9. There is a strong tendency for the adjacent background to be almost devoid of any CCs above 20 mJy in the surrounding regions as well as regions that exist between clusters of strong CCs ≤ 0.1 mas across in the east west direction. The north-south resolution is worse making the constraint on the north-south distribution of CCs comprising the WN and EN more subjective in nature. The north-south distributions of CCs in Figures 4, 7, 8 and 9 also seem to naturally cutoff at a size < 0.15 mas, similar to the resolution of the longest north-south baselines ($\sim 0.13 - 0.14$ mas).

The details of our CC models of the WN and EN can be found in Table 2. The first two columns are the date of the observation and the number of days since the nuclear separation was first detected. This is not the same as the time from the epoch of physical separation due to the finite resolution of the array. The next two columns are the flux densities of the WN, EN and the total of these numbers, respectively. The absolute flux calibration accuracy of the BU data is about 5% (Jorstad et al. 2017)³. Column 5 provides the properties of the uniformly weighted beam on top and the naturally weighted beam below in parenthesis. Column (6) is the peak intensity from the CLEAN images (Figure 2) for comparison with the numbers in the previous columns. Columns (7) and (8) are the largest magnitude negative contour values from the CLEAN image and the CC cutoff used in our models, respectively. Columns (9) - (11) are the uncertainties in the nuclear separation that are computed per the methods of Section 3.2.

First, let us consider the epoch of August 26 2018. Since the absolute astrometry is lost in the phase self-calibration step of the VLBI data reduction, we are only interested in the relative positions of the EN and WN and we place the brighter WN at the origin. We include all the CCs within a region ≤ 0.1 mas in the east-west direction. The blue (red) ellipse encircles all the CCs that are associated with the EN (WN). The EN involves considerably weaker CCs than the WN and the distribution tends to be more elongated in the north-south direction. This is typical during the first year of our monitoring of the time evolution of the nuclear region. The May 12 2019 observation in the top righthand side of Figure 4 shows a larger separation between the EN and WN.

The bottom two panels of Figure 4 show the emergence of a third component in the fall of 2019. It was clearly seen in the October 2019 observation, but the SNR was poor so we show the high SNR epochs of November 2019 and January 2020. The bottom right hand panel shows that the centroids of the three clusters of CCs (see the next subsection) are nearly colinear. Thus, it makes sense to consider them all part of the same flow. As such, we tentatively relabel the three components as follows. Based on the early epochs, the WN is associated with the point of origin. It is the brightest feature in 2018 and the much weaker EN seems to flow out of the partially resolved cluster in the time frame of August to December. We therefore consider the EN as the first ejection, or ejection A. In the fall of 2019, the new feature shown inside the green ellipse is about half the brightness of the EN and WN, we call it ejection B. We actually never see it separate from the WN, so this scenario is not verified, but suggested by the pattern evolution. We cannot rule out that the red ellipse represents a new ejection in the western direction and the green component is the point of origin. This is disfavored because it would require the EN to be contracting towards the point of origin and the point of origin would change from being a much brighter component than the EN to much fainter than the EN.

3.2. *The Position of the Features*

We calculate the position of the features by taking the flux-density weighted mean (centroid) of the CC positions in the feature. In Figure 4, the red triangle inside the red ellipse and the blue triangle inside the blue ellipse are the locations of the centroids of the flux density of the CCs encapsulated within each ellipse. We assign an uncertainty to the centroid location. The origin of the coordinates

³ Normally, the VLBA-BU-BLAZAR fluxes are accurate to within $\sim 5\%$, but from early 2019 to September 2019 it is quite a bit more uncertain, at least 30%, because of pointing errors. Given the diffuse nature of 3C 84, we can only roughly estimate corrections through use the Metsähovi monitoring program fluxes at 37 GHz (for a description of the Metsähovi monitoring, see Teräsraanta et al. 2004). The VLBA resolves out too much of the structure to do that accurately, as we can for more compact sources.

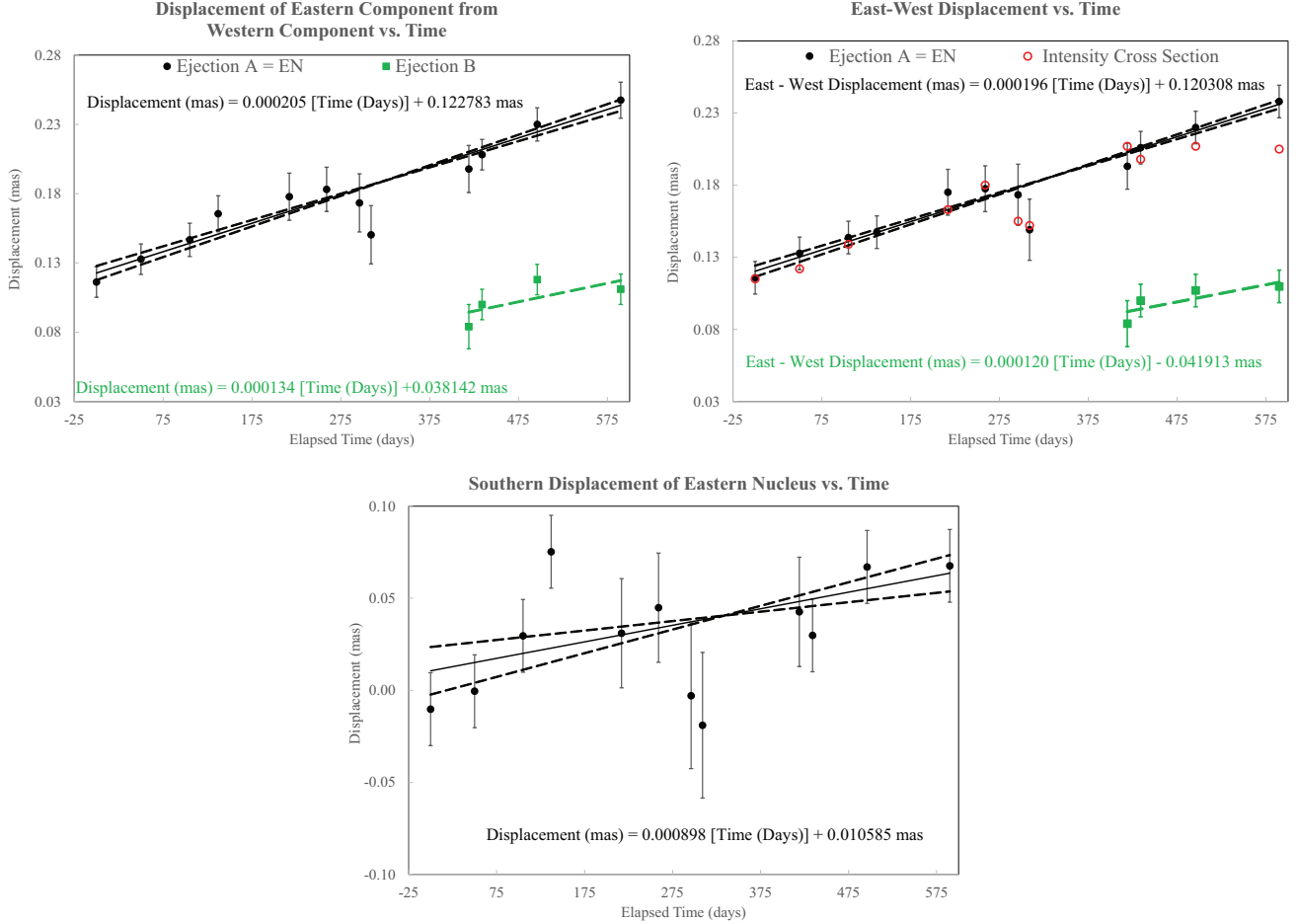


Figure 5. The separation between WN and EN versus time is demonstrated in two ways. The top left panel is a plot of total displacement versus time. The east-west displacement is plotted in the top right panel. The two methods yield a similar separation velocity. The solid black line is a least squares fit with uncertainty in the vertical variable (Reed 1989). The dashed lines define the standard error of the fit. The equation for the best fit is printed on the plot. We also provide a crude fit for ejection B in green. The top right panel also plots the east-west separation from the intensity profiles (in red) with no information from January 10, 2019 available from Figure 3. We consider these data less rigorous and are shown as a consistency check. The peak separation of the intensity cross-sections lies below the uncertainty of the CC model fit for April 2020 (day 590). This is a consequence of a curved trajectory of the EN. As can be seen in Figure 2, the EN starts veering south relative to the declination of the WN in 2020 and is most pronounced in April. Thus, there is no east-west cross section that captures intensity peaks of both the EN and WN. The April data indicates the breakdown of the simple east-west cross section method for a curved trajectory for the ejection. For completeness, we include the southern displacement of the EN with its fit in the bottom panel. The magnitude of the trend is small compared to the uncertainties and this is reflected in the standard error of the best fit. Thus, the result should be viewed with caution. The three outliers are January 10, 2019 (that is discussed in Appendix B) and the two low SNR observations in June and July 2019.

will be the centroid of the WN and all displacements are measured relative to this. The uncertainty in the positional locations is $\sim 10\%$ of the synthesized beam FWHM for these bright components

(Lister et al. 2009)⁴. In Table 2, the uncertainties in coordinate separation, $\sigma_{\Delta X}$ and $\sigma_{\Delta Y}$ (X is right ascension and Y is declination), are the uncertainties on the individual centroid coordinates added in quadrature. Similarly, the uncertainty of the total displacement between the EN and WN, σ_D , is calculated as the error propagation of the centroid uncertainties. The random noise contribution to the separation uncertainty can be estimated by $\sigma_D(\text{noise}) \approx 0.5 d \sqrt{\sigma_{\text{rms}}/S_{\text{peak}}}$, where σ_{rms} is the post-fit rms noise of the image and S_{peak} is the flux density of a putative unresolved component of size d (Fomalont 1999; Lee et al. 2008). $\sigma_{\text{rms}} < 1$ mJy for all epochs except June and July 2019 where it is closer to 2 mJy. We determine in Table 2 that $S_{\text{peak}} > 479$ mJy so all the SNR are > 500 except June 2019 which is $\gtrsim 400$. It is therefore clear that positional uncertainty is not dominated by the random noise component. The error estimate adopted in Table 2 is much more conservative than stochastic noise errors and incorporates systematic uncertainty.

4. THE SEPARATION RATE OF THE DOUBLE NUCLEUS

The motivation for defining the locations of the EN and WN and the corresponding uncertainty is to track the time evolution of the separation of the components. This is performed in Figure 5. The top left panel is the plot of the displacement versus time. However, we note that the displacement is primarily east-west and the highest resolution is in this direction. We plot east-west (x direction) displacement in the top right panel for direct comparison to the intensity cross-sections in Figure 3.

The data were fit by a least squares fit with uncertainty in the vertical variable (Reed 1989). The solid line is the fit and the dashed lines represent the standard error to the fit. Based on the fit and standard error, the time averaged nuclear separation speed is $0.086 \pm 0.008c$. The fit to the total displacement yields a separation rate of $73 \pm 7 \mu\text{as}$ per year compared to $70 \pm 6 \mu\text{as}$ per year for pure east-west displacement. Note that we also plot (in green) the separation of the second ejection, ejection B, in the lower right hand corner of the two panels. We also provide very crude four point fits to the ejection velocity.

It is apparent that the EN-WN separations in the spring and summer of 2019 (days 217 – 309) deviate from the least squares fits in Figure 5. This is not unexpected from the Tables 1 and 2. These are the most compromised observations. However, the July 2019 estimated separation lies particularly far from the fit. It is possible to explain this behaviour to be due to the ejection “B” that is shown in the bottom frames of Figure 4. This central component is resolved from EN and WN in our CC cluster models first in October 2019, but it is most likely present already in earlier epochs. If this is indeed the case than we may just not resolve it in July 2019, but it is there and it blends with WN, moving its measured position slightly towards EN. This can cause the small inward motion seen at that epoch. The results of this paper do not rely on this interpretation.

By considering the east-west displacement, we are able to directly compare the results of the intensity profile description in Figure 3 with the CC models of the EN and WN in Section 3. The distribution of intensity cross-section separations is generally consistent with both the standard error of the least squares fit and the uncertainty of the CC model fits to the EN-WN separation (the measurement uncertainty given in Table 2) except for two regions, in June and July 2019 for which the SNR was poor and the last two points, January and April 2020. Figure 2 and the bottom frame of Figure 5 seem to indicate that beginning in January 2020, the EN no longer appears to follow a predominantly east-west trajectory, but begins to veer southward towards the southerly directed

⁴ see also <https://science.nrao.edu/facilities/vla/docs/manuals/oss/performance/positional-accuracy>

large scale jet. The EN appears to propagate in a southeasterly direction rather than an easterly direction. Thus, a pure east-west cross section is unable to properly capture the intensity peaks of both components. The situation is more extreme in April and this could cause the measurement using the intensity cross section to be less than the true east-west displacement. This circumstance illustrates the limitation of the simple east-west cross section method of measuring separation if the trajectory curves.

For the sake of completeness, we plot the southern displacement of the EN as it separates from the WN in the bottom panel of Figure 5. The putative trend is far less pronounced than the east-west separation and the uncertainty is much larger (the synthesized beam is elongated in this direction). Consequently, there is no robust quantitative assessment that can be made due to the limitations of the CC based method of this paper.

One can also perform a long extrapolation back in time (assuming that the separation velocity was approximately constant in time) of the linear fits in order to find the epoch of zero separation from the nucleus. From Figure 5, we have that ejection A, the WN, emerged on January 1, 2017 with a large uncertainty that places it anywhere between September 21, 2016 and March 22, 2017. We can crudely estimate the zero separation epoch for ejection B from Figure 5 as \sim November 6, 2017. The two ejections originated at least 7 months apart and represent two distinct nuclear events. Our estimate of the January 1, 2017 ejection is not tightly constrained, but we would be remiss not to mention that there was a major gamma ray flare reaching TeV energies that was detected by the Large Area Telescope on board the Fermi satellite and MAGIC telescopes that peaked around December 31, 2016 to January 1, 2017 (Baghmany et al. 2017; Ansoldi et al. 2018).

5. THE DOUBLE NUCLEUS IN THE UV-PLANE

It is customary for astronomers to fit the visibility data with a small number of Gaussians in the order to track component separations. Thus, we explore the possibility of evidence of the double nucleus in the (u, v) plane by making Gaussian fits to the nuclear region. However, there are two concerns for this method in the context of the separating nuclear features in Figure 2. Firstly, the radio source 3C 84 is extremely complex compared to a typical blazar nucleus and it is extended. So, one needs to use a CC model to represent it, but that creates a problem regarding how large of an area around the core should be cleared from CCs before model-fitting. This is always a bit subjective and can influence the results significantly. The second issue is that the initial stages of the expansion in Figure 2 are at the limits of the resolution of the VLBA. There is no unique solution to the fitting method. Each ambiguity and assumption adds a possible error to the fitting process. After some initial attempts to make Gaussian fits to the nuclear region we found two methods that give reasonable results.

5.1. *Gaussian Fitting Method 1*

The first method addresses the issue of the complex background emission by a simple excision method that can be uniformly applied to each epoch. We took the CLEAN model and automatically removed CCs from the area three times the uniformly weighted beam size (from Table 2) around the core. The excised region is then modelled with circular Gaussians. We added new components in the model if a clear peak was seen in the residual image after fitting. The background subtraction is not perfect so it introduces additional Gaussian components in addition to those associated with

Table 3. Gaussian Fits to the Double Nucleus

(1)	(2)	(3)	(4)	(5)	(6)	(7)	(8)	(9)
Date	Model	$F_{\nu,WN}$	$F_{\nu,EN}$	ΔRA	Δdec	Separation	Gaussian FWHM WN	Gaussian FWHM EN
		(Jy)	(Jy)	(mas)	(mas)	(mas)	(mas)	(mas)
08/26/2018	1	1.137	1.437	0.093	0.046	0.104	0.073	0.156
08/26/2018	2	1.146	0.840	0.135	0.001	0.135	0.068	0.102
10/15/2018	1	2.525	1.138	0.157	-0.053	0.166	0.104	0.127
10/15/2018	2	2.219	1.459	0.146	-0.008	0.146	0.088	0.134
12/09/2018	1	3.211	1.435	0.166	-0.027	0.168	0.113	0.052
12/09/2018	2	2.819	1.856	0.151	-0.034	0.155	0.085	0.082
01/10/2019	1	1.179	4.634	0.139	0.019	0.140	0.085	0.190
01/10/2019	2	2.030	2.321	0.127	0.018	0.128	0.076	0.072
03/31/2019	1	1.193	1.576	0.169	-0.009	0.169	0.068	0.132
03/31/2019	2	1.819	0.932	0.166	0.022	0.167	0.066	0.071
05/12/2019	1	2.735	0.593	0.200	-0.007	0.200	0.143	0.018
05/12/2019	2	2.601	0.786	0.199	-0.043	0.204	0.119	point source
06/18/2019	1	2.794	0.970	0.170	-0.010	0.170	0.091	0.011
06/18/2019	2	2.470	0.795	0.151	0.018	0.152	0.074	0.107
07/01/2019	1	2.716	1.961	0.162	0.007	0.162	0.019	0.055
07/01/2019	2	3.876	2.032	0.151	0.028	0.153	0.071	0.029
10/19/2019	1	2.505	1.629	0.183	-0.066	0.195	0.155	0.100
10/19/2019	2	1.284	1.454	0.221	-0.026	0.223	0.091	0.092
11/03/2019	1	0.688	1.041	0.234	-0.040	0.237	0.063	0.053
11/03/2019	2	1.193	1.120	0.222	-0.031	0.224	0.061	0.042
01/04/2020	1	1.370	1.109	0.232	-0.066	0.242	0.104	0.059
01/04/2020	2	1.222	1.523	0.240	-0.064	0.249	0.075	0.081
04/07/2020	1	2.517	0.706	0.264	-0.111	0.286	0.144	point source
04/07/2020	2	1.878	1.286	0.262	-0.080	0.274	0.109	0.046

the EN, WN and ejection B. This method typically needs many components to represent the core, which can make the fit unstable.

5.2. Gaussian Fitting Method 2

We took the CLEAN model, but removed only those CCs that roughly correspond to the double (triple) nucleus in a super-resolved image (created with a 0.1 mas circular beam). This CC excision was done “by eye”, so there is some subjectivity here. We modelled this region with 2 or 3 circular Gaussian components. The method is less subjective than the first as a result of incorporating additional information from the super-resolved image. However, the method relies significantly on the CLEAN model, and it is therefore not independent.

5.3. Comparison of Methods

In Figure 6 we reproduce Figure 5 with the addition of the separation derived from the Gaussian models of the nuclear region described above. There are two things to note. First of all, the east-west separation in 2018 and early 2019 displayed in the bottom panel deviates much more from the cross-sectional method of Figure 3 than the CC approach used in this paper. Secondly, because Model 2 is derived using super-resolved images, it agrees better with the CC model data. The Gaussian fits to the EN and WN are listed in Table 3. The two fits can be compared to each other as well as the CC based method in Table 2. There are some large differences in the flux density of the EN and WN between the two models in columns (3) and (4). This might be a consequence of the different methods of removing the background and the relatively large Gaussian FWHM in columns (8) and (9) that are comparable to the separations in column (7). If we perform a linear fit to the separation

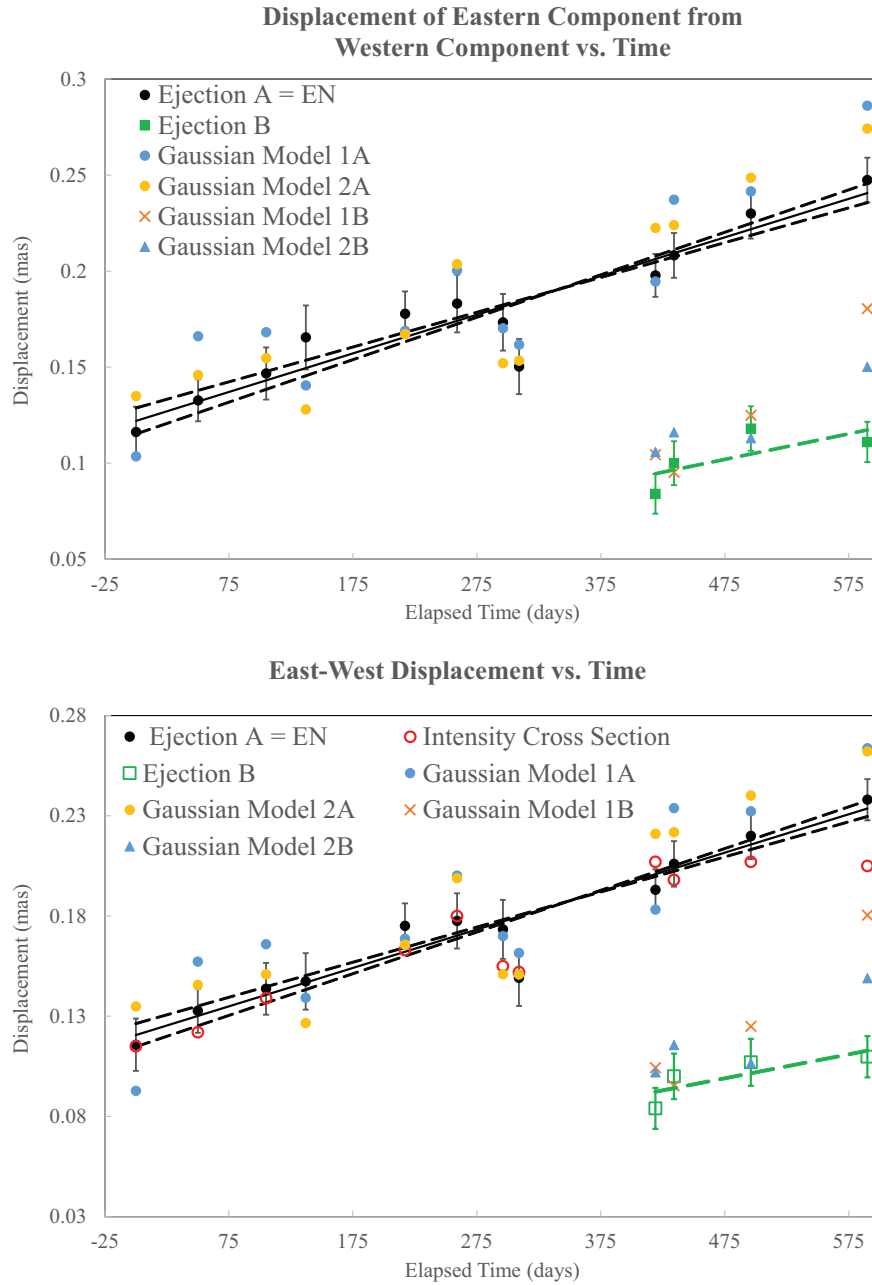


Figure 6. The Gaussian components produced by the Difmap fit in the visibility domain are indicated by blue and orange symbols, for Method 1 (described in Section 5.1) and Method 2 (described in Section 5.2). These are overlaid on the plots from Figure 5. Method 1A and 2A points are the distances from the Gaussian representing the EN from the Gaussian representing the WN. Similarly, method 1B and 2B points are the distances from the Gaussian representing the ejection B from the Gaussian representing the WN. We do not present error bars on the Gaussian fit data since it would clutter the graph making it unintelligible.

from the Gaussian fit we find a similar separation rate for both Gaussian fitting schemes, about 15% larger than what was found in Section 4, $0.100c$. This is surprising considering that on a point by point level the agreement is not that tight.

In Figure 7, the Gaussian components for both models given in Table 3 are overlaid on CC distribution for two adjacent epochs. We define EN and WN as in Figure 4. The image is qualitative, but it gives the reader a feel for the difference between the two model results and the difference between the models and the CC based methods. Method 2, which utilizes information from the super-resolved images, seems very consistent with the EN and WN identifications in May 2019. Figure 6 and Tables 2 and 3 indicate some significant discrepancies between the results of the CC method of Sections 3 and 4 and the Gaussian models during the epoch April 7, 2020. This is most pronounced for ejection B. In Figure 8, we overlay the Gaussian fits on the CC scatter plot from Figure 4. There is clearly disagreement between the two fits. Furthermore, Model 1 seems to blend the EN and ejection B and Model 2 seems to ignore all the CCs at the north end of the EN. This suggests that the Gaussian fit methods have difficulty resolving 3 components within a total extent of 0.24 mas . The figure clearly shows the origin of the larger displacements for ejection B in the April 2020 epoch of Figure 6 given by the Gaussian models compared to the CC based analysis.

The main objective of this study is to track the time evolution of the double separation as close to its inception as possible in order to estimate the trajectory and separation speed as accurately as possible. There is arbitrariness in the Gaussian fitting procedure that is accentuated in the early epochs (in 2018) when the component separation was smaller. The intensity cross-sections were introduced in Figure 3 to provide a clear diagnostic of the model fitting schemes. Based on Figure 6, both Gaussian decomposition schemes give worse fits to the east-west separation derived from the intensity cross-sections in the early epochs than the CC based methods of Section 3 and 4. We do not advocate extrapolating the Gaussian fitting method to the first three epochs of small component separation. Similarly, Figure 8 seems to indicate that the second ejection crowds the narrow 0.24 mas field making it difficult for the Gaussian fits to segregate components uniquely or with high accuracy. For this reason, we consider the CC method of this paper preferable to conventional Gaussian fitting for exploring the partially resolved compact nuclear region of 3C 84. The Gaussian fitting does provide qualitative agreement with CC model fitting. As such, along with the intensity cross-sections, this corroborates the results of the CC based analysis. We have also demonstrated that with proper care in the definition of the Gaussian models, one can achieve a similar estimate (within 15%) to the nuclear separation.

6. THE NUCLEAR SEPARATION IN THE CONTEXT OF RADIOASTRON

In order to create more context for these results in 2018-2020, we compare the nuclear structure to the triple nucleus observed on September 21-22, 2013 by RadioAstron (Kardashvev et al. 2013, 2017). First of all, the RadioAstron observations were accompanied by a 43 GHz observation with an array of the VLBA combined with the phased VLA (Giovannini et al. 2018, Savolainen et al., in prep.). We use the clean component model from imaging of these data together with the methods of this paper to detect evidence of a triple nucleus using the east-west resolution of the VLBA. There were no September or October observations by the BU monitoring program. The top panel of Figure 9 is a nuclear clustering model similar to Figure 4. It shows all the CCs $> 20\text{ mJy}$ in a nuclear region that is a square, 0.4 mas on a side. Without the RadioAstron results, this compact configuration would have been more ambiguous to decompose into three components. Based on the RadioAstron images,

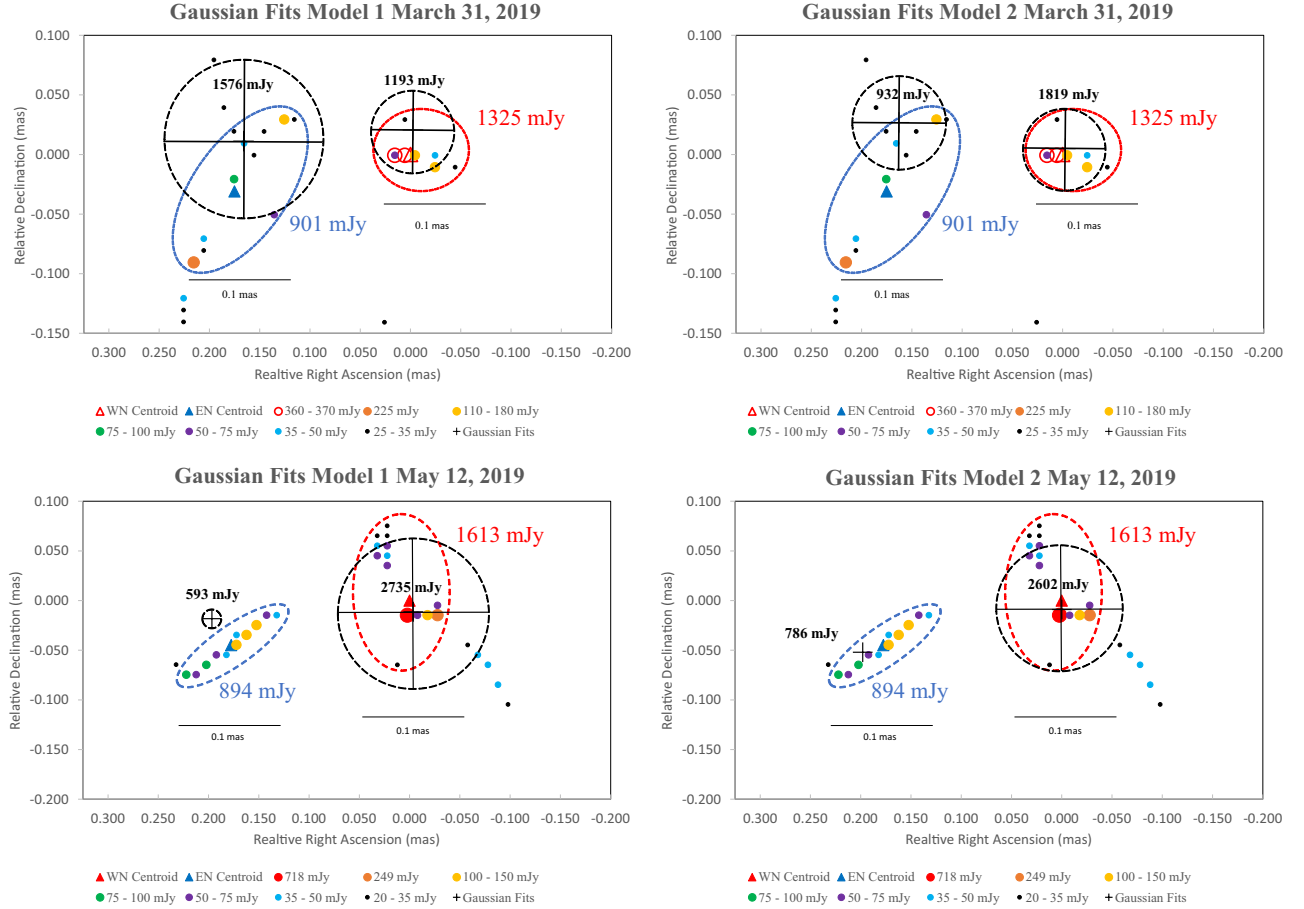


Figure 7. The foreground Gaussian components from Table 3 are indicated by the dashed black circles with the inscribed black crosses. Both Model 1 (described in Section 5.1) and Model 2 (described in Section 5.2) are plotted, but separately for clarity. The diameter of the circle represent the FWHM of the Gaussian component. These are superimposed on the CC component models as defined in Figure 4. The flux densities are in black near or inside each Gaussian component. The eastern component of Gaussian Model 2, in May, is a point source and it is represented by a black cross.

we cluster the CC components into three regions of concentration, RA East (blue), RA Central (red) and RA West (green). The nuclear region is very clean, there are relatively few CCs compared to the other epochs considered and the background CC field is sparse near the triple nucleus in the innermost 0.2 mas. This fortuitous circumstance facilitates the identification of the components of the triple nucleus. The distance from RA East to RA Central is ≈ 0.08 mas and RA Central to RA West is ≈ 0.09 mas.

We overlay the locations of the RA East, RA Central and RA West as blue, red and green triangles, respectively from the top panel on the RadioAstron image. The locations appear to be close to what is expected from the 22 GHz image. The flux densities of the RA East, RA Central and RA West are 456 mJy, 2106 mJy and 845 mJy, respectively in the 43 GHz CC decomposition of the top panel of Figure 9. Gaussian fits to the nuclear region of the RadioAstron data yield flux densities of the RA East, RA Central and RA West of 564 mJy, 775 mJy and 389 mJy, respectively at 22 GHz. RA

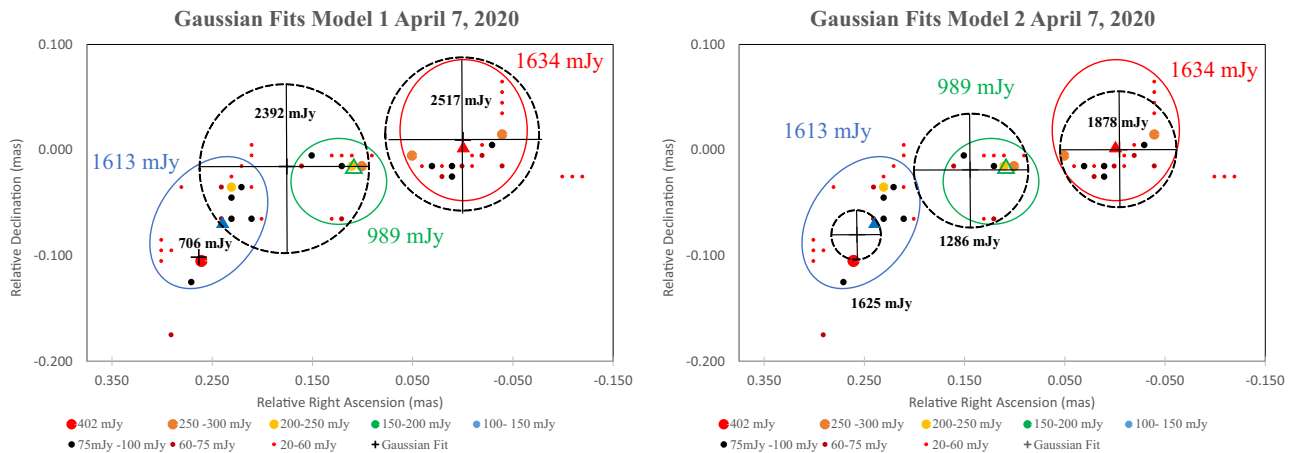


Figure 8. The figure compares the Gaussian models with the CC derived components during the epoch April 7, 2020. The figure is formatted the same as Figures 4 and 7. The three bright components in close proximity to each other seems to provide a challenge for the Gaussian models as evidenced by the significant differences between the models from methods 1 and 2. The eastern component of Gaussian Model 1 is a point source and it is represented by a black cross. We have not included the 0.1 mas rulers in this figure in order to avoid distracting clutter.

Central and RA West have a highly inverted (rising) spectrum between 22 GHz and 43 GHz either from synchrotron self-absorption or from free-free absorption (Walker et al. 2000).

We try to assess the degree to which the nuclear region has changed in terms of morphology and size in 2018-2020 compared to 2013. The cross-identification of components is rather uncertain due to 5 years between the observations. We cannot make any robust cross-identifications of the components from epoch to epoch due to the known variability of the morphology and the effects of blending with low resolution. We simply give two plausible cross-identifications in the bottom panel of Figure 9 and Figure 10 to help elucidate the large qualitative changes that might be occurring over time. First, we identify the brightest component of VLBA with the brightest component of RadioAstron. With this chosen scenario, we tentatively identify RA Central as the same physical feature as the WN in Figure 4. We also overlay the locations of the EN in August 26, 2018 and May 12, 2019 on the RadioAstron image in the bottom panel of Figure 9. In this cross-identification scenario, the nuclear structure has widened by $\sim 40\mu\text{as}$ and the whole pattern is shifted to the east.

The first cross-identification scenario is straightforward, but just one of many possible choices. Thus, in Figure 10 we show a different plausible cross-identification based on the high SNR January 4, 2020 observation of the nuclear triple. The color coding of the triangles corresponds to the color coding in the CC model in the bottom right hand panel of Figure 4. Note that the triangles have a different identification than in Figure 7. In this scenario the nuclear structure has widened by $\sim 60\mu\text{as}$ and the point of origin of the ejections is the red triangle at the far west edge of the jet. The triple axis is tilted relative to September 22, 2013. In summary, both the interpretation in Figure 9 and Figure 10, indicate a highly dynamic nuclear region that evolved to a wide state in 2019. The physical identification of the components is not obvious, but our time evolution study clearly identified luminous plasma ejected towards the east.

7. CONCLUSION

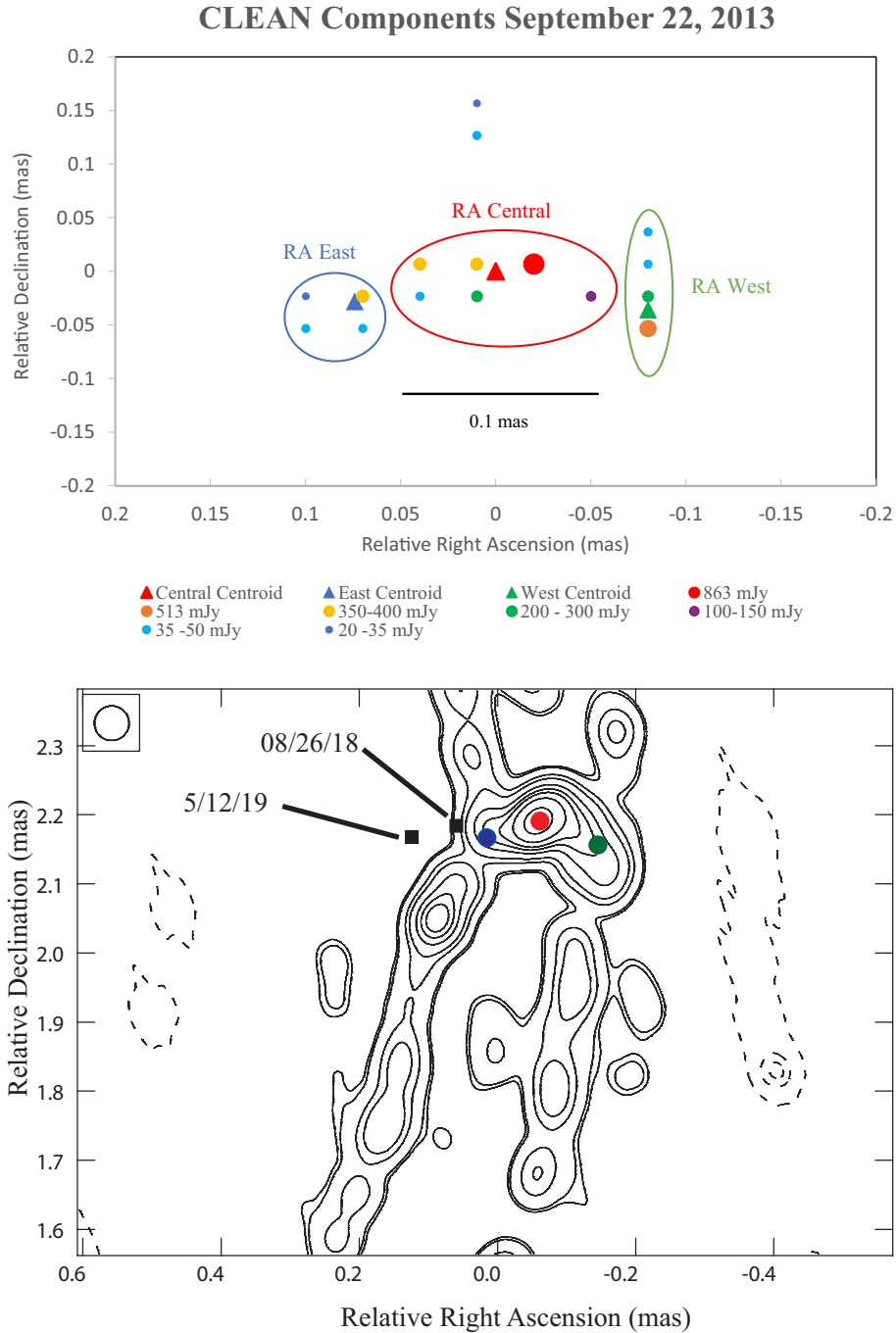


Figure 9. The top panel shows the location of the nuclear CCs > 20 mJy on September 22, 2013 based on a 43 GHz VLBA plus phased VLA observation that was quasi-simultaneous with the 22 GHz RadioAstron observation in the bottom panel. We cluster the CCs as three physical components RA East (blue), RA Central (red) and RA West (green). Their positions are overlaid on the RadioAstron image from [Giovannini et al. \(2018\)](#). We cross-identify the brightest component, RA Central, with the bright component in 2018/2019, the WN. Based on this identification, we also show the positions of the EN in August 26, 2018 and May 12, 2019 relative to the RadioAstron image in the bottom panel. The contour levels are (-10, -7.50, -3, 7.500, 10, 30, 50, 100, 150, 200, 300, 500)mJy.

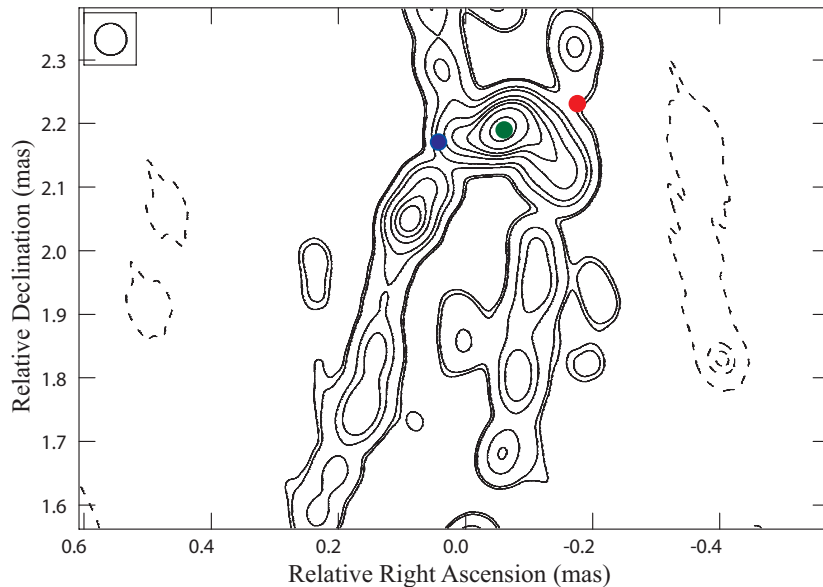


Figure 10. We consider an alternative (to Figure 9) cross-identification of components between our 43 GHz VLBA monitoring of the multiple nucleus and the RadioAstron image. This interpretation is based on the CC model for January 4, 2020 in the bottom right hand panel of Figure 4. There is a triple nucleus in that epoch as well. The color coding of the centroid locations are the same as in Figure 4. One very significant difference is that in January 2020 the central component is the weakest and in September 2013 it is the brightest. The multiple nucleus is wider in 2020. The contour levels are (-10, -7.50, -3, 7.500, 10, 30, 50, 100, 150, 200, 300, 500)mJy.

In this paper, we consider three methods for resolving the nuclear structure in 43 GHz VLBA observations of 3C 84, intensity cross-section, Gaussian fitting in the (u, v) plane and CC models. The time averaged separation speed from August 2018 to April 2020 is estimated as $0.086 \pm 0.008 c$. A second ejected component was identified in October 2019 to April 2020 with a similar speed. The multiple nucleus has been detected before with RadioAstron and 86 GHz global VLBI, but the dynamical evolution has never been seen previously. This separation speed estimate accomplishes the primary goal of this paper.

The most relevant comparison are the component measurements at the base (inner ~ 0.2 mas) of the 43 GHz VLBA southerly directed jet (Dhawan et al. 1998). They found apparent velocities in the range $0.035 c - 0.1 c$. However, there was uncertainty in the identification of the location of nucleus. Independent of any of the nuclear identification scenarios, the apparent velocity was slow by relativistic standards $\lesssim 0.1 c$, very similar to what was found in this study of the multiple east-west nucleus. The apparent jet speed accelerates as the jet propagates southward with $\sim 0.25 c$ at ~ 1 mas and the highest estimates approach $0.47 c \sim 2$ mas away (Suzuki et al. 2012).

It is tempting to try to understand the observed motion in the context of the complicated circum-nuclear structure depicted in Figure 1. However, we choose not to speculate and use our result as one piece of the puzzle that must be incorporated into future efforts to explain the base of the jet in 3C 84. It is certainly odd to see an inner flow or expansion that appears to be orthogonal to the large scale jet that is clearly delineated only $150 \mu\text{as}$ downstream (Giovannini et al. 2018; Kim et al. 2019). One thing that we can say is that the double separation is ~ 0.3 lt-yrs on the sky plane in April 2020.

This corresponds to an intrinsic distance of $\approx 0.3/\sin\theta$ lt-yrs, where θ is the line of sight (LOS) angle to the component motion. This equates to $\sim (1900/\sin\theta)M$ where $M \sim 10^9 M_\odot \sim 1.5 \times 10^{14}$ cm is the black hole mass in geometrized units (Nagai et al. 2019; Punsly et al. 2018; Scharwachter et al. 2013). Thus, this slow apparent separation speed persists very far from the source. The LOS angle has been estimated at $11^\circ - 65^\circ$ based on jet/counter-jet asymmetry (Walker et al. 1994; Asada et al. 2006; Lister et al. 2009; Fujita and Nagai 2017). However, these viewing angle estimates are for the north-south jet. The direction of the east-west core motion may differ significantly from this. It is perhaps more relevant that historical data indicates that 3C 84 sometimes appears moderately blazar-like based on broad band variability and optical polarization as high as 6% (Veron 1978; Angel and Stockman 1980; Chuvaev 1985; Nesterov et al. 1995). In current nomenclature, it is a slightly “off angle blazar” at times (Punsly et al. 2018). For the sake of comparison, estimates for blazars are typically $\theta \approx 1^\circ - 3^\circ$ (Hovatta et al. 2009; Jorstad et al. 2017). However, the blazar-like properties have been far more benign for the last 35 years (Punsly et al. 2018). As an example, in the last 12 years the optical polarization has been consistently between 1%-3% with the very rare jumps to 4%⁵. So we cannot rule out $\theta \sim 10^\circ$, but this behavior does not favor an extreme blazar-like line of sight. Based on the published ranges of θ , the physical distance between the EN and WN is $\sim 0.3 - 1.5$ lt-yrs, or $\sim 1900M - 9800 M$. What is extremely odd is that at this large distance, the VLBA images seem to indicate a dramatic change in the jet direction. The most straightforward interpretation is that we are detecting the internal dynamics of a jet that is $\sim 2000 M$ wide. The lateral expansion near the central engine proceeds sub-relativistically at $\sim 0.086c$. The jet is collimated on scales $> 2000 M$. The RadioAstron image and the April 2020 image in Figure 2 seem to indicate a continuous flow between the central, wide core component and bright components moving along the edges of the jet going south.

Based on RadioAstron and this analysis, the bifurcating nuclei are bright ejections of plasma that can go primarily to the east or west. In the epochs considered here there is an ejection to the east. In 2020, the images in Figure 2 appear to show that the EN trajectory starts to bend toward the south. It might be joining the highly collimated portion of the jet that is directed almost due south. However, this is not so simple based on Figure 2 because the western ridge is much brighter at this time. The ejection might traverse (twist around) the front face of the southerly directed jet and join the western ridge.

The discussion above shows how confusing the dynamics of the inner jet are likely to be. Considering the variations in the ridge brightness distribution over time, suggests that the jet dynamics are not even consistent from epoch to epoch. A year long series of target of opportunity, 43 GHz relative astrometry VLBA observations of > 8 hours with two calibrators triggered by a > 0.15 mas separation of the nuclear double could be a feasible method of tracking the time evolution of the ejections accurately. The observations could be triggered by a separation determined by the methods of this paper from the BU data. Perhaps 86 GHz observations with global VLBI (including the Atacama Large Millimeter Array) spread out over 6 months that are triggered simultaneous with the VLBA observations might shed light on what kind of dynamics are occurring. These are challenging observations, but this might be one of our best laboratories for studying the base of a powerful extragalactic jet.

⁵ <http://www.bu.edu/blazars/VLBAproject.html>

ACKNOWLEDGMENTS

This study makes use of 43 GHz VLBA data from the VLBA-BU Blazar Monitoring Program VLBA-BU-BLAZAR funded by NASA through the Fermi Guest Investigator Program⁶. The Very Long Baseline Array (VLBA) is an instrument of the National Radio Astronomy Observatory. The National Radio Astronomy Observatory is a facility of the National Science Foundation operated by Associated Universities, Inc. TS was supported by the Academy of Finland projects 274477 and 315721. HN is supported by JSPS KAKENHI grant No. JP18K03709.

REFERENCES

- Angel, J. and Stockman, H. 1980, *ARA&A* 18, 321
- Ansoldi, S., Antonelli, L., Arcaro, C. et al. 2018, *A&A* 617, 91
- Asada K., Kamenno S., Shen Z.-Q., Horiuchi S., Gabuzda D. C., Inoue M., 2006, *PASJ*, 58, 261
- Baghmanyan, V., Gasparyan, S., and Sahakyan, N. 2017, *ApJ* 848 111
- Blandford, R. and Königl, A. 1979, *ApJ* 232 34
- Chael, A., Narayan, R., Johnson, M. D. 2019, *MNRAS* 486, 2873
- Chuvaev, K. 1985, *PAZh* 111, 803
- Dhawan, V., Kellermann, K. I., Romney, J. D. 1998, *ApJL*, 498, 111
- Fomalont, E. 1999, in *Synthesis Imaging in Radio Astronomy II*, ASP Conference Series, eds. Taylor, G., Carilli, C., Perley, R. 180, 301
- Fujita, Y. and Nagai, H. 2017, *MNRAS*, 465, L94–L98
- Giovannini, G., Savolainen, T., Orienti, M. et al. 2018, *Nature Astronomy* 2, 472
- Hada, K., Giroletti, M., Kino, M., et al. 2014, *ApJ*, 788, 165
- Hardcastle, M., Evans, D. and Croston, J. 2009, *MNRAS*, 396, 1929
- Hodgson, J., Rani, B., Lee, S.-S. et al. 2018, *MNRAS* 475 368
- Hovatta, T., Valtaoja, E., Tornikoski, M., Lähteenmäki, A. 2009, *A&A* 498, 723
- Jorstad, S., Marscher, A., Morozova, D., et al. 2017, *ApJ*, 846, 98
- Kardashev, N. S., Khartov, V. V., Abramov, V. V. et al. 2013, *Astronomy Reports* 57, 153
- Kardashev, N. S., Alakoz, A. V., Adrianov, A. S. et al. 2017, *Solar System Research* 51, 535
- Kim, J.-Y., Krichbaum, T., Lu, R.-S., Ros, E. et al. 2018 *A&A* 616 188
- Kim, J.-Y., Krichbaum, T. P., Marscher, A. P., et al. 2019, *A&A*, 622, 196
- Lee, S.-S., Lobanov, A., Krichbaum, T. P. et al. 2008, *ApJ*, 136, 59
- Lightman, A., Press, W., Price, R. and Teukolsky, S. 1975, *Problem Book in Relativity and Gravitation* (Princeton University Press, Princeton)
- Lind, K., Blandford, R. 1985, *ApJ* 295, 358
- Lister, M. L. 2001, *ApJ*, 562, 208
- Lister, M. L., Cohen, M., Homan, D. et al. 2009, *AJ* 138, 1874
- Marscher, A. P. 1985, in *Supernovae as Distance Indicators*, *Lecture Notes in Physics*, 224, 132
- Martí-Vidal, I.; Perez-Torres, M. A., Lobanov, A. P. 2012 *A & A* 541 A135.
- Mościbrodzka, M., Falcke, H., Shiokawa, H. 2016 *A & A* 586 38
- Nagai, H., Suzuki, K., Asada, K., Kino, M., Kamenno, S. et al. 2010, *PASJ* 62, L11
- Nagai, H., Haga, T., Giovannini, G., et al. 2014, *ApJ* 785, 53
- Nagai, H., Onishi, K., Kawakatu, N., et al. 2019, *ApJ* 883, 193
- Narayan R., Yi I., 1994, *ApJL*, 428, 13
- Nesterov, N., Lyuty, V., Valtaoja, E. 1995, *A&A* 296, 638
- Pedlar, A., Ghatuare, S., Davies, R. et al., 1990, *MNRAS* 246, 477
- Punsly, B., Marziani, P., Bennert, V., Nagai, H., Gurwekk, M., 2018, *ApJ* 869, 143
- Punsly, B. 2019, *ApJL* 879, 11
- Reed, B. 1989, *Am. J. Phys.* 57 642
- Rees, M. J. 1966, *Nature* 211, 468
- Scharwachter, J., McGregor, P. J., Dopita, M. A., Beck, T. L. 2013 *MNRAS* 429, 2315
- Suzuki, K., Nagai, H., Kino, M., et al. 2012, *ApJ* 746, 140
- Teräsranta, H., Achren, J., Hanski, M. et al. 2004, *A&A* 427, 769

Trippe, S., Krips, M., Pietu, V., et al. 2011, A&A
533, 97
Veron, P. 1978, Nature 272, 430
Walker R. C., Romney J. D., Benson J. M., 1994,
ApJ 430, L45

Walker R. C., Dhawan V., Romney J. D.,
Kellermann K. I., Vermeulen R. C., 2000, ApJ
530, 233
Wright, E. L. 2006, PASP, 118, 1711
Yuan F., Narayan R., 2014, ARA&A 52, 529

APPENDIX

A. THE RESOLUTION LIMITS OF THE VLBA OBSERVATIONS

The ability to resolve structures in interferometric data depends on several factors, e.g., the length of the longest baselines, gaps in the (u, v) coverage, signal-to-noise ratio of the data, and the complexity of the source structure itself. Giving an accurate number for any given experiment requires simulations of that exact experimental setup and the source. Therefore, one usually resorts to simple rules of thumb like the fringe spacing, the uniformly weighted beam size or the criterion we have adopted for the current paper. Since all the observations we consider have similarly high SNR and similar complexity of the source structure, it is reasonable to assume that any variation in the resolution limit from epoch to epoch is mainly due to the longest baselines available. Since we use only epochs that have either MK-SC baseline or MK-HN baseline present, the variation in the maximum baseline length in E-W direction is only $\sim 15\%$. The important question is, whether our adopted resolution limit of $0.08 - 0.10$ mas is on average correct for the VLBA in the high SNR case. We explore this by means of simulations in the visibility domain.

Using AIPS task UVMOD we simulated visibility data with exactly the same (u, v) coverage and noise properties as in the August 2018 observation, the epoch of minimum detectable separation with our CC based method presented in this paper. As an input model, we used the August 2018 CC model. From this CC model, we excised an area of 3 uniform beam sizes (FWHM) around the core. To the resulting model, we added two 1 Jy point sources separated from the origin symmetrically in relative RA by ± 0.02 mas. The independent variable in this experiment is the separation in relative RA, the horizontal axis in Figure 11, measured in mas. We created eight simulated data sets increasing the separation between the point sources from 0.04 mas to 0.18 mas in steps of 0.02 mas. Then we used the MODELFIT task in Difmap to fit the visibility data with a model consisting of two point sources in the core region. After making the fit, we plotted the two dependent variables of the experiment, the flux ratio and the fitted separation of the components in Figure 11, the vertical axis in the top and second panels, respectively. At separations of 0.04 mas and 0.06 mas, the fitted data do not accurately represent the real separation nor the real brightness ratios. At 0.08 mas, this abruptly changes to precise fits to both quantities. It clearly shows that two equally bright point sources can be resolved, if their separation is 0.08 mas or larger.

We also made a second set of simulations with the same input model. However, instead of point sources we used two 1 Jy Gaussian distributions with a FWHM of 0.1 mas each. Recall from Section 3.1, there were 20 estimates of the FWHM of the components that range from 0.023 mas to 0.112 mas with a mean of 0.076 mas. The fitting in Difmap was made with point sources as in the previous experiment. The results are presented in the third and the bottom panels of Figure 11. It seems that separations of $0.10 - 0.12$ mas ($\sim 10\%$ accuracy in the separation) or larger are needed in this case to accurately estimate the relative positions. We note that the smallest measurable distance with our CC method in Table 2 is 0.116 ± 0.013 mas in August 2018. Not coincidentally, the value obtained by the simulation. We also note that the analysis of the simulations used an inexact model of the flux distributions. This analysis seems consistent with the model-fitting in the (u, v) plane in Figure 6. When compared to the CC model method, the model fits seem less accurate with higher model dependence for separations less than ~ 0.13 mas.

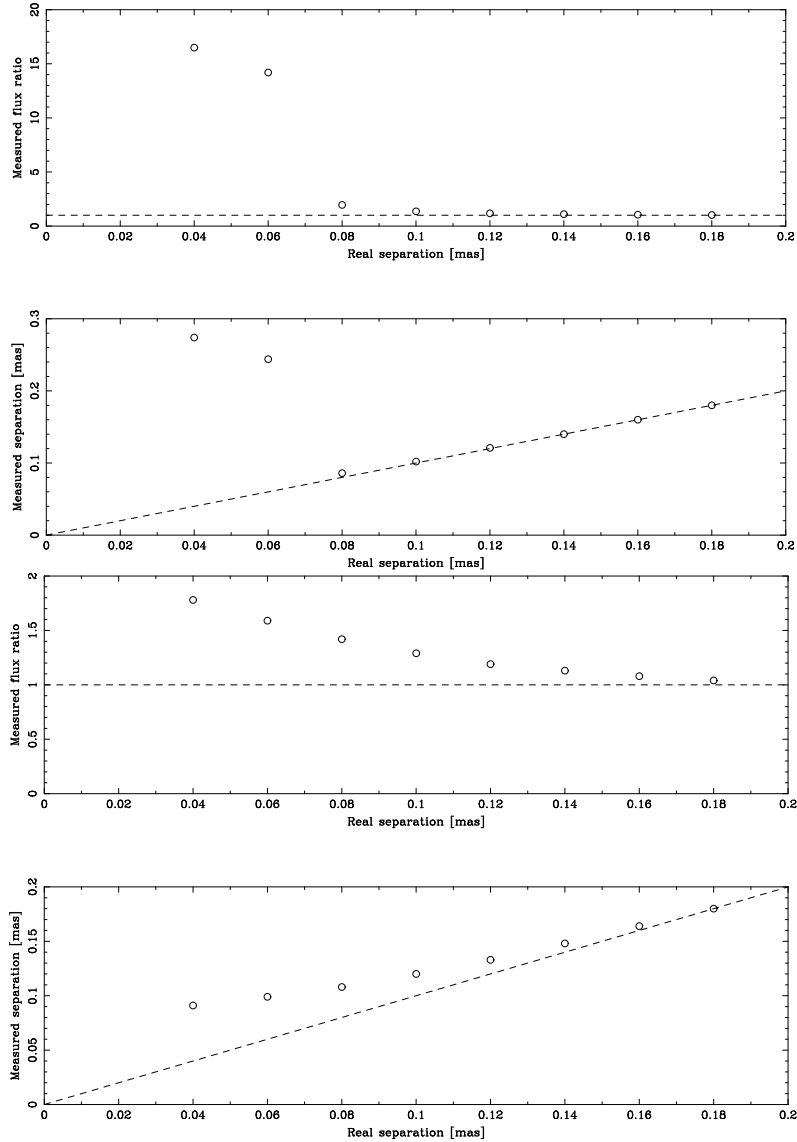


Figure 11. The results of our simulations in the (u, v) plane. The horizontal axes are the separation between our two injected nuclear components. The vertical axes are the model-fitted values of the flux ratio (for which the ground truth is one by construction) and the separation of the two fitted components. The top two panels are for the point source experiment described in the text. Accurate model fitting occurs for a separation of > 0.08 mas. The bottom two frames are for Gaussian sources with a FWHM of 0.1 mas. In this case a slightly larger separation is required for accurate model-fitting in the (u, v) plane.

B. THE CC MODEL FROM JANUARY 10, 2019

The January 10, 2019 intensity profile looks different than the adjacent epochs in Figure 3. It has one peak instead of two. Thus, this epoch needs to be studied in detail. From Section 2, we repeat the fundamental philosophy of implementing CC models “Even though the models may not be robust in a single epoch, they should be suitable for identifying a trend that persists over time, especially with regards to very bright features as is the case here.” We use this as our guide for assessing what has occurred during this epoch.

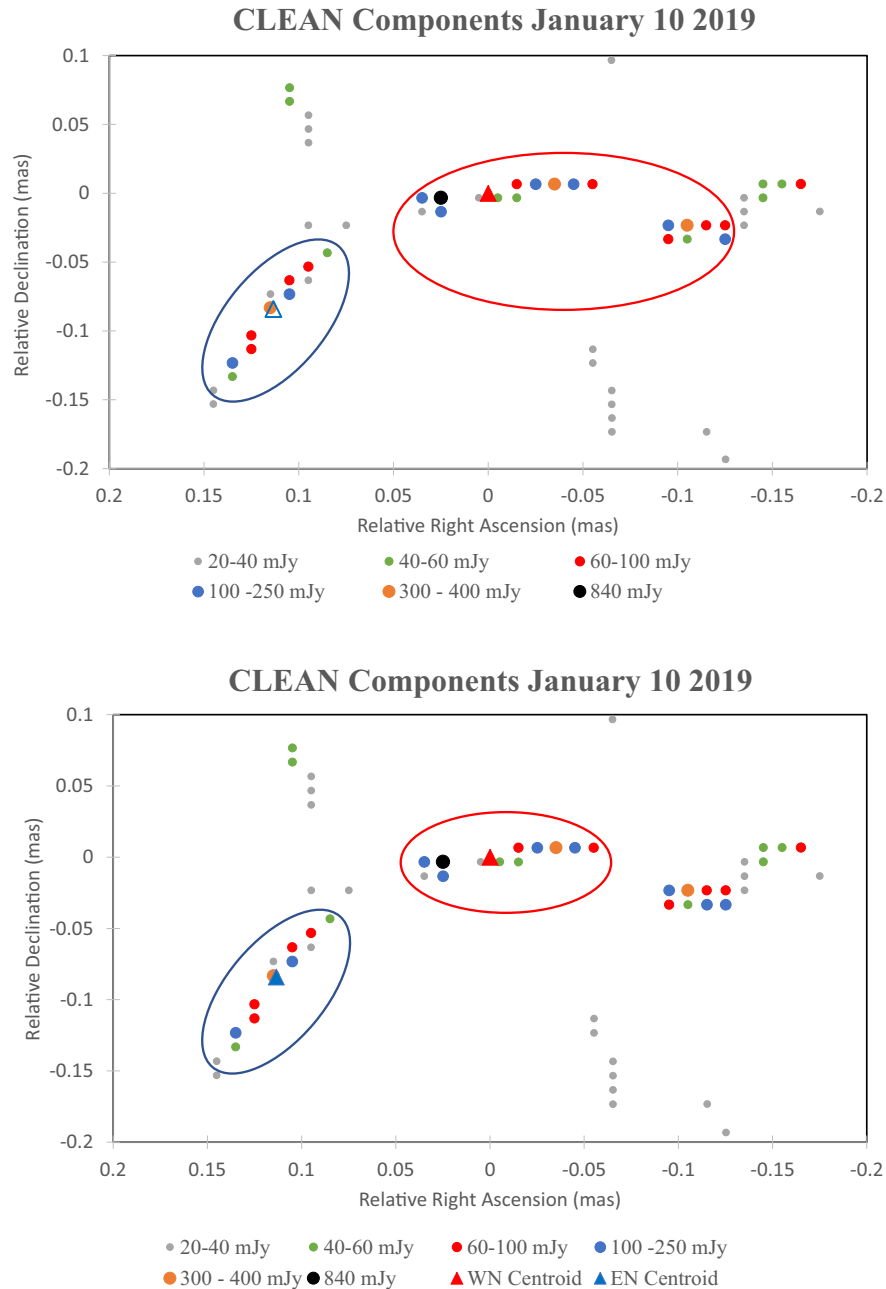


Figure 12. The distribution of CCs from the January 10, 2019 data reduction on the BU website. The figure format is the same as Figure 4. Two models are presented for the CC clustering. The top one is the one used in the main text and Figure 5 and is referred to as Model 1 for the clustering of the CCs. Model 2 is the bottom frame.

Figure 12 is an analog of Figure 4 that displays the distribution of CCs. The figure considers two plausible decompositions into a WN and EN. The single peak structure of the intensity profile is explained by the figure, the EN lies to the south of the WN by $\lesssim 0.1$ mas. Thus, it is not captured by the intensity cross section that is centered on the peak intensity (near the centroid of the WN). The other odd feature is the core now appears to have a bright feature emitted to the west. This is

slightly to the south of the intensity peak and appears as an inflection point in the western skirt of the intensity profile in Figure 3. Such a feature would be consistent with the nuclear triple detected by RadioAstron (Giovannini et al. 2018). Our main task in this Appendix is to investigate if these two features, the southern displacement of the EN and the western new component, are accurate reconstructions of the source or affected by artifacts of the observation and/or the CC model.

The first thing to consider is the quality of the observations. January 10, 2019 appears to be a good epoch with all 10 antennas operating normally, only with MK and Pie Town (PT) taken out for the last 2 scans of 3C84 for use by the Navy. Thus, we look for other indicators of the root cause of the morphological change bearing in mind the fundamental qualifying assumption of using the CC models that was restated at the beginning of this Appendix.

Do the other epochs tell us anything? None of the other epochs, including the one just before in December or the one after in March have a EN this far south relative to the WN nor do they have an ejection to the west. The putative ejection to the west is very bright (1.095 Jy), brighter than the EN, so why does it not appear in March and May? Such rapid changes could occur with blazar-like phenomena. However, we are seeing a steady mildly relativistic separation of the nucleus in Figure 5. If we treat the changes in the CC model in January as real then it would imply an abrupt change from this slow (by relativistic standards) steady nuclear separation to one in which the EN veers south and a bright component is ejected west. Then in March it appears to be an extrapolation of the slow, steady separation that was occurring from August to December. The EN pops back up to the north, similar to previous epochs, and the bright west ejection disappears and this basic structure persists in May. This is not impossible (and would be very interesting), but it is not supported by any other evidence that we have. This would correspond to the bottom identification of CC clustering for the EN and WN in Figure 12. We will refer to the bottom frame in Figure 12 as Model 2, since it is not our preferred model.

The CC clustering model (Model 1) in the top frame of Figure 12 assumes that the western bright spot is not a new ejection or background feature, but is separated from the peak intensity possibly as an artifact of the (u, v) coverage. Thus, the two features are combined into one feature that is stretched out in the east-west direction in this interpretation. Similarly, the southward veer of the EN would be a result of imperfect (u, v) coverage and calibration. The disturbing aspect for our method is that instead of the east-west separation of the CCs comprising the WN being ~ 0.1 mas, it is 0.16 mas. We were motivated to prefer this interpretation by the smooth transition to and from the epochs adjacent to it in time. Model 1 is used in Figure 5. This model has a displacement that is fairly close to the least squares fit in both panels of Figure 5.

Now, we can compare this with Model 2. We show the fits in Figure 13 that are the analogs of those from Figure 5, but we have substituted Model 2 for Model 1 in Figure 5. The fits are similar to Figure 5, but Model 2 lies very far from the least squares fit of the east-west displacement. Thus, Figures 5 and 13 favor Model 1 over Model 2 based on the trends of the other epochs.

The anomalous intensity cross-section in Figure 3 and the ambiguity in the component decomposition (two or three components) of the nucleus is disturbing considering that this observation had all 10 stations. In order to investigate this further, we tried re-imaging the (u, v) data with CLEAN + self-cal since the end result of the image reconstruction depends on the “route” that is taken during the imaging process for imperfect data (i.e., sampling is poor and/or data has significant gain errors). The resultant images are sensitive to the initial phase self-cal steps and we were able to redistribute

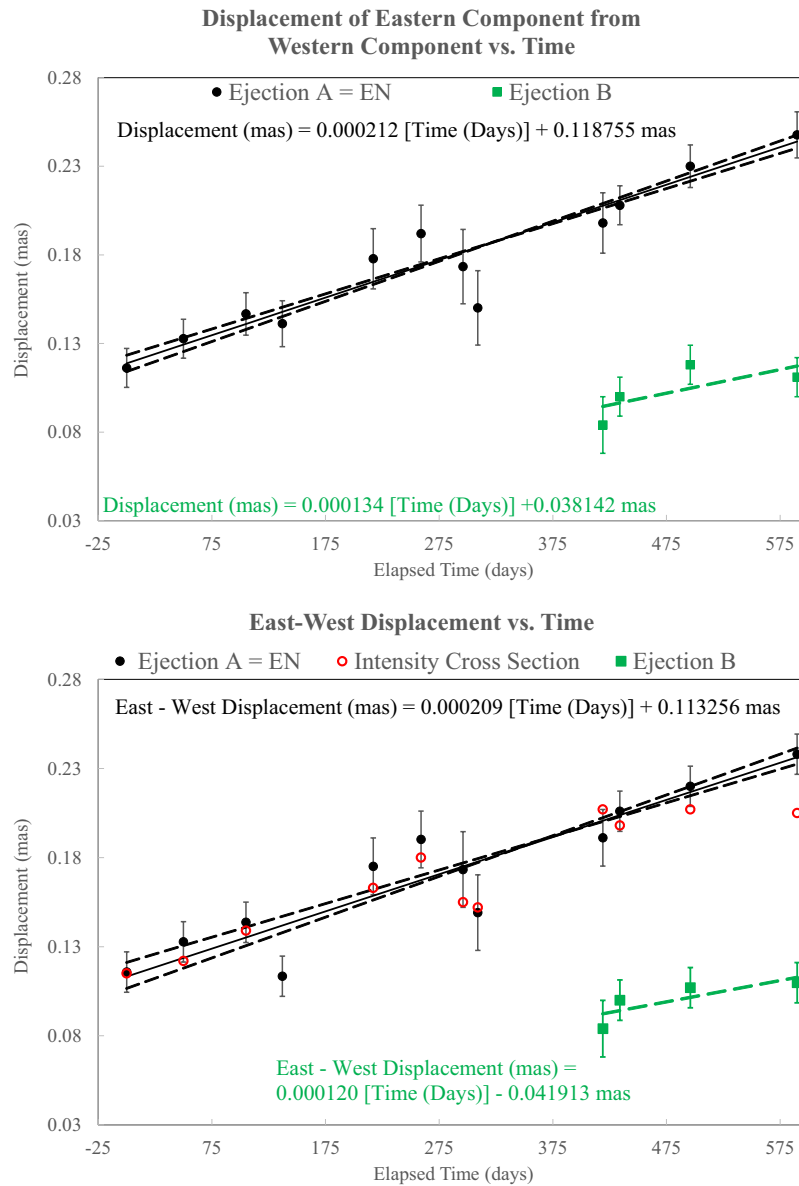


Figure 13. Figure 5 is recreated, but instead of using Model 1 from the top panel of Figure 12, we use Model 2 from the bottom panel of Figure 12 to estimate the double nucleus separation speed.

the CCs in the image plane. However, none of the images had an intensity cross section that was “in-family” with the cross section expected from Figure 3 (i.e., 2 well defined, distinct peaks). Furthermore, none of the images resolved the ambiguity between a two component decomposition of the nucleus or a three component decomposition of the nucleus. Similar to Figure 12, the EN-WN separation was always in the range 0.13 mas to 0.17 mas, regardless of the self calibration or the particular choice of the identifications of the CCs with the EN and the WN. It is therefore concluded that the “out of family” properties of the January 2019 observation are inherent to the (u, v) data and are not an artifact of image reconstruction. The re-imaging investigation does not address whether this

is a physical property of the source at the time of observation or an idiosyncrasy of this particular patchy sampling in the (u, v) plane.

We hypothesize, without proof, the plausibility of (u, v) coverage issues with the observation. 3C84 is a very complex source with many components. The (u, v) data sampling is not ideal for such a complex source, as it is being observed with 31-32 other sources over a 24 hour period. The (u, v) coverage is not the same in all epochs. Occasionally, the (u, v) coverage might not be sampled well enough to reconstruct the complex structure adequately or uniquely. We cannot prove if the image is accurate or adversely affected by patchy (u, v) coverage. Our basic premise is that we cannot vouch for the integrity of the CC models in an individual epoch, but we can detect temporal trends in the bright components. To this point, the results of our analysis do not depend on choosing Model 1 over Model 2. The estimated separation velocity with the choice of Model 1 in Figure 5 was $0.086 \pm 0.08 c$. By comparison, using Model 2 (as was done in Figure 13), results in almost exactly the same separation velocity $0.088 \pm 0.007 c$. Thus, our results do not depend on the confusing details of a particular epoch.